Aeolian Research 2 (2010) 5–26

Contents lists available at ScienceDirect

Aeolian Research

journal homepage: www.elsevier.com/locate/aeolia

Light scattering and absorption by wind blown dust: Theory, measurement, and recent data

Haley E. Redmond, Kathy D. Dial, Jonathan E. Thompson *

Department of Chemistry and Biochemistry, MS1061, Texas Tech University, Lubbock, TX 79409, USA

ARTICLE INFO

Article history:
Received 6 July 2009
Revised 22 September 2009
Accepted 28 September 2009

Keywords:
Dust
Refractive index
Light scattering
Measurement
Optical properties

ABSTRACT

Large quantities of dust with diameters <10 μm are dispersed in earth's atmosphere by wind-driven processes. This dust is of significant scientific interest owing to its ability to potentially alter climate, reduce local visibility, cause respiratory problems in humans, and affect biogeochemical cycles in the world's oceans. In this work, we present a review of the theory of light scattering and absorption by small particles, discuss common measurement techniques used to characterize the optical properties of airborne particulates, and summarize recent measurements of the optical properties of airborne dust. For the review of recent measurements we focus on the visible and near IR properties of dust, and present Angstrom exponents, real and imaginary parts of refractive index, and single scatter albedo data obtained and published by other authors for a variety of locations in the Northern Hemisphere dust belt and Australia.

1. Introduction

Aeolion processes are major sources of particulate matter (PM) present in earth's atmosphere. Indeed, recent estimates place annual emission fluxes for mineral dust aerosols with diameters <10 μm around 1–3 Pg yr^{-1} (Peta = 10^{15}) (Textor et al., 2006). An additional 2–10 Pg of sea-salt particles are produced annually with a significant portion of this mass resulting from particles produced when wind-generated waves/whitecaps break (Lewis and Schwartz, 2004). While dust aerosols are generally produced in arid or semi-arid regions, the particles that are suspended in the atmosphere can be transported large distances from the source region. For instance, episodes of Saharan dust transported to the Caribbean or southeastern United States have been documented (Toon, 2003). These dust clouds are thought to affect both climate and iron deposition into the world's oceans (Jickells et al., 2005; Mahowald et al., 2005). Similarly, transport of dust/aerosols across the Pacific has been shown to affect regional air quality in the western United States (Jaffe et al., 1999; Jaffe et al., 2003a; Jaffe et al., 2003b; Fairlie et al., 2007).

Both mineral dust and sea-salt aerosol can have significant impacts on air quality/chemistry, human health, both regional and global climate, and local visibility. For instance, NO_2 can be taken up on mineral oxide particle surfaces and metal oxide particles are believed to catalyze the decomposition of ozone (Usher et al., 2003; Miller and Grassian, 1998; Cwiertny et al., 2008). Mineral dust particles are also known to serve as effective ice nuclei (Salam et al., 2006; Zuberi et al., 2002.). Increased particle mass loadings have been correlated with human mortality rates and respiratory distress (Sarnat et al., 2000; Olson and Boison, 2005). Also, wind-dispersed particles scatter and absorb light in the atmosphere causing decreases in visibility. Visibilities of only a few meters have been encountered in extreme circumstances. The absorption and/or scattering of light by nanometer–micrometer sized particles can potentially alter atmospheric photochemistry and affect regional climate. For instance, some models have implied that heating of the atmosphere aloft caused by light absorption by soot may have altered precipitation patterns in China (Menon et al., 2002). A similar effect could be envisioned for absorbing wind-blown dust aerosols. Indeed, recent work has suggested the "Dust Bowl" drought of the 1930's may have been amplified by the effects of the dust aerosols that serve as the hallmark of this era (Cook et al., 2009).

In this work, we present a review of light scattering and absorption by particulate matter. Sections 2 and 3 of the review provide an overview of the theory of light scattering and absorption by particulate matter. Section 4 summarizes experimental techniques for the measurement of light scatter/absorption by aerosols. Both well-established methods and recent developments in the field will be discussed. Finally, observations of pertinent optical properties of dust aerosols presented in the literature will be compiled and presented in Section 5.

2. Light scattering and absorption by single particles

2.1. Interaction of particles with light

Fig. 1 illustrates several possible phenomenon which can occur when a beam of electromagnetic radiation of wavelength λ_0 and

---

* Corresponding author. Tel.: +1 806 742 3210; fax: +1 806 742 1289.
E-mail address: jon.thompson@ttu.edu (J.E. Thompson).

1875-9637/$ - see front matter © 2009 Elsevier B.V. All rights reserved.
doi:10.1016/j.aeolia.2009.09.002

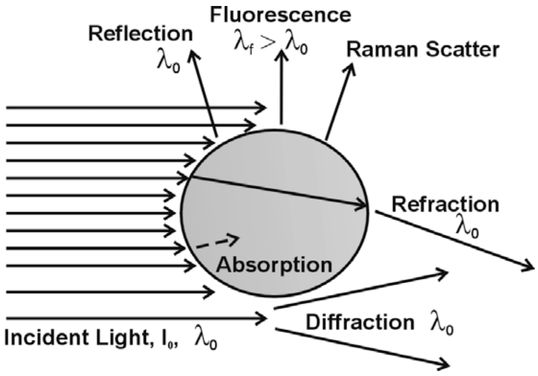

Fig. 1. A depiction of potential optical interactions between incident radiation and a particle.

irradiance I_0 (W/m^2) is incident upon a particle. The cumulative effects of reflection, refraction, and diffraction comprise elastic scattering. In elastic scattering, photons in the incident beam are redirected from their original path without a change in photon energy ($\lambda_0 = \lambda_{\text{scatter}}$). Absorption of light by the particle can also occur. In this case, the absorbed energy can be re-radiated as thermal emission, or possibly fluorescence. While the former is believed to be the dominant process, certain aerosol particles/layers have been found to be fluorescent (Immler et al., 2005; Pan et al., 2007). This is not surprising given many components of airborne particulates such as polycyclic aromatics, humic-like substances, and cells/cellular debris are known to fluoresce. Inelastic Raman scatter can also occur, although this phenomenon is generally much weaker than elastic scattering. This section of the review will focus on elastic scatter and light absorption by small spherical particles.

If a beam of irradiance I_0 (W/m^2) is incident on a particle such as that illustrated in Fig. 1, a simple geometric model would allow prediction that the particle could absorb and scatter light incident upon it and cast a "shadow" in its wake. The net loss of light energy from the beam is called extinction. Extinction is the sum of the effects of elastic scattering and absorption. The absolute energy removed from the beam can be modeled as:

$$I_{ext} = I_0 \times \sigma_{ext} \tag{1}$$

where:

$$\sigma_{ext} = \sigma_{scat} + \sigma_{abs} \tag{2}$$

where I_{ext} (W) is the amount of light energy removed from the beam, and σ_{ext}, σ_{scat} and σ_{abs} represent terms known as the extinction, scattering, and absorption cross sections for the particle in question (m^2). Now at first glance, the σ terms might appear to simply be the particle's geometric cross sectional area. This is not the case. The σ terms can in fact be much smaller than or even exceed the cross sectional area of the particle. In fact, values of σ can be 4-5 times larger than a particle's cross sectional area resulting in the *extinction paradox* – the concept that a particle can remove more light from a collimated beam than what is actually incident upon it (this is a consequence of diffraction).

The scattering/absorption/extinction cross-sections (σ) for a particle is defined as the product of a particle's physical cross-sectional area and a term represented by Q

$$\sigma_{ext} = Q_{ext} \times \pi r^2 \tag{3}$$

$$\sigma_{scat} = Q_{scat} \times \pi r^2 \tag{4}$$

$$\sigma_{abs} = Q_{abs} \times \pi r^2 \tag{5}$$

In these equations r represents the particle radius and the Q terms (unitless) are known as the single particle extinction, scattering, or absorption efficiency parameter depending on which effect is described. Again, at first glance it might seem the value for Q could not exceed 1, since this would imply a given particle could remove more light from a beam than what is incident upon it. However typical values of Q range from well less than 1 to around 4. Single scatter albedo (ω) is taken as the ratio of the scattering and extinction cross sections or the corresponding Q terms:

$$\omega = \frac{\sigma_{scat}}{\sigma_{ext}} = \frac{Q_{scat}}{Q_{ext}} \tag{6}$$

For a given particle, the value of Q is a complex function of particle size, wavelength of light, and complex refractive index of the particle. The refractive index (m) of a material is defined as the ratio of the speed of light in vacuum (c) to the speed of light in that material (v):

$$m = \frac{c}{v} \tag{7}$$

Since the speed of light is lower in materials when compared to vacuum, the value of $m > 1$. The value of refractive index loosely scales with the density of the material under study and is typically 1.3–2 for most atmospheric aerosols. For particles that absorb light, refractive index is expressed as a complex number ($m = n + ik$) consisting of a real (n) and imaginary part (k) which describe the optical properties of a given particle. The real part helps describe the scattering behavior of the particle and the imaginary part (k) describes the extent of light absorption. Refractive index varies with wavelength and often increases with decreasing wavelength. Knowledge of complex refractive indices for aerosols is very important since this parameter and particle size are the only intrinsic properties required to model optical properties of spheres.

Another important variable that helps describe a given particles optical properties is its size. This is usually done through the particle size parameter (α). The particle size parameter is the ratio of a particle's circumference to the wavelength of probe light:

$$\alpha = \frac{2\pi r}{\lambda} \tag{8}$$

The theory and calculations pioneered by Gustav Mie over 100 years ago can be employed to provide exact solutions for scattering/absorption of light for any spherical particle at any wavelength if α and refractive index is known. A detailed discussion of these calculations is well-beyond the intended scope of this review and we would direct the reader to the works of Bohren and Huffman, or Kerker for a more detailed mathematical description of Mie's theory (Bohren and Huffman, 1983; Kerker, 1969).

It is often convenient to consider certain particle size ranges for which approximations can be employed. Particles that are small compared to the probe wavelength ($\alpha \leqslant 0.2$) fall under the domain of Rayleigh scattering. Particles which have roughly the same diameter as the wavelength of light ($0.2 \leqslant \alpha \leqslant 10$) fall in the Mie regime and optical properties must be obtained via Mie theory. Particles with diameters which are large compared to the probe wavelength ($\alpha > 10$) fall into the geometric optics domain in which classical laws of reflection, refraction, and diffraction are often suitable for description of particle optical properties.

2.1.1. Efficiency parameters for Rayleigh scatter

Most dusts that result from wind-driven processes are far too large to be considered Rayleigh scatterers of visible light. However, these particles could be treated as such when interacting with long wavelength electromagnetic radiation. Thus, this section is included in this review in the spirit of comprehensiveness. When an electromagnetic wave interacts with a particle which is very small, the particle will experience an electromagnetic field which appears approximately uniform over the dimensions of the particle. This creates an oscillating electric dipole, coupled to the electromagnetic wave that re-radiates that frequency in all directions. The single particle extinction, scattering, and absorption efficiency parameters for sufficiently small particles can be given as (Bohren and Huffman, 1983; Hinds, 1999):

$$Q_{ext} = 4\alpha \mathrm{Im}\left\{\frac{m^2-1}{m^2+2}\left[1+\frac{\alpha^2}{15}\left(\frac{m^2-1}{m^2+2}\right)\frac{m^4+27m^2+38}{2m^2+3}\right]\right\} + \frac{8}{3}\alpha^4 \mathrm{Re}\left\{\left(\frac{m^2-1}{m^2+2}\right)^2\right\} \qquad (9)$$

$$Q_{scat} = \frac{8}{3}\left(\frac{\pi d}{\lambda}\right)^4\left(\frac{m^2-1}{m^2+2}\right)^2 \qquad (10)$$

$$Q_{abs} = 4\alpha Im\left\{\frac{m^2-1}{m^2+2}\right\}\left[1+\frac{4}{3}\alpha^3 Im\left\{\frac{m^2-1}{m^2+2}\right\}\right] \qquad (11)$$

The term “Re” indicates the real part of refractive index, while “Im” denotes the imaginary part. Eq. (10) illustrates Rayleigh scattering efficiency is strongly coupled to particle diameter (d^4). Also, the $1/\lambda^4$ relationship suggests a strong wavelength dependence of scattering with shorter wavelengths being scattered more efficiently. Indeed, this relationship helps answer the age old question of why the sky is blue! Rayleigh scatter is also generally believed to be unaffected by particle shape, a condition which is clearly not met for larger particles.

2.1.2. Angular dependence of Rayleigh scatter

If a collimated, unpolarized beam of intensity I_0 and wavelength λ illuminates a Rayleigh particle of diameter d, the angular intensity profile $I(\theta)$ of the scattered radiation can be given as:

$$I(\theta) = \frac{I_0\pi^4 d^6}{8R^2\lambda^4}\left(\frac{m^2-1}{m^2+2}\right)^2(1+\cos^2\theta) \qquad (12)$$

where R is the distance from the particle, m is refractive index, and θ scattering angle. Fig. 2 defines the coordinate system commonly used to define scattering angle. Light scattered between 0 and 90° is said to be forward scattering and light scattered 90–180° is back scatter. Angles between 180 and 360° are usually not considered for spheres since scatter is symmetrical about the *xz* plane. The angular dependence of Rayleigh scatter is clearly contained within the $(1 + \cos^2\theta)$ term. Rayleigh scattering is symmetrical in the forward and reverse directions, and maximum scatter intensity is observed at 0, 180° and a minima at 90° referenced to the incident beam. This phenomenon is best observed in a diagram of the angular scattering pattern for a Rayleigh particle as illustrated in Fig. 3 ($\alpha = 0.1$ in figure). The minima/maxima observed occur as a result of the polarization state of the scattered light. For unpolarized incident light, the intensity of scattered light polarized perpendicular to the scatter plane can be given by:

$$I_\perp = \frac{I_0\pi^4 d^6}{8R^2\lambda^4}\left(\frac{m^2-1}{m^2+2}\right)^2 \qquad (13)$$

This equation indicates light polarized perpendicular to the scatter plane is scattered isotropically, that is evenly in all directions. Alternatively, the intensity of light scattered with polarization parallel to the scattering plane is given as:

$$I_\parallel = \frac{I_0\pi^4 d^6}{8R^2\lambda^4}\left(\frac{m^2-1}{m^2+2}\right)^2(\cos^2\theta) \qquad (14)$$

Eq. (14) suggests the intensity of the parallel polarized component is 0 at 90° scatter angle. Indeed, light scattered by a very small particle is completely polarized perpendicular to the scatter plane at an angle of 90°.

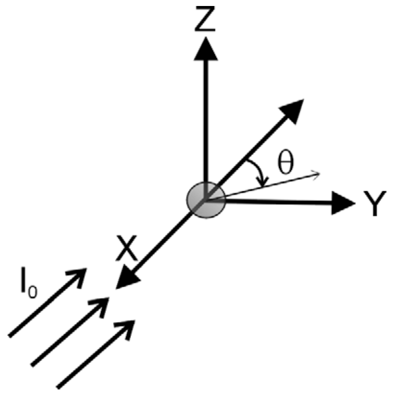

Fig. 2. Cartesian coordinate system defining scattering angle (θ). The incident beam is aligned with the *x*-axis approaching in the direction of the arrows. The angle between the direction of the incident beam and scattered beam in the *x*, *y* plane is the scattering angle (θ). The scattering particle is located at the origin. Scattering at angles near 0° represents a small deflection of light from its original path while 180° would represent light scattered back towards the source.

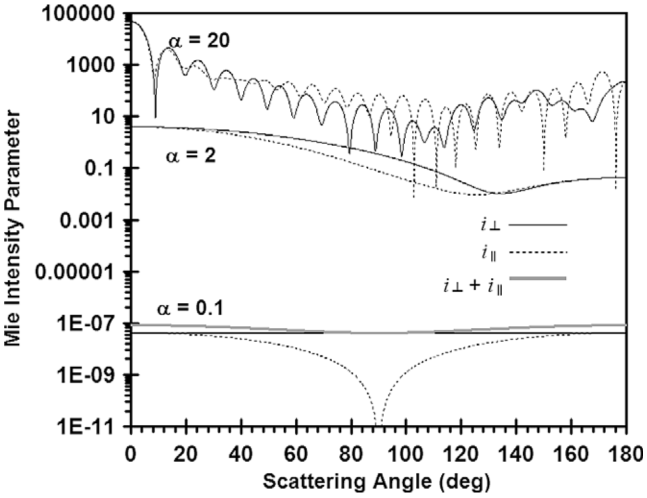

Fig. 3. Mie intensity parameters for perpendicular and parallel polarizations plotted as a function of scattering angle for a water droplet ($m = 1.33$) of size parameters 0.1, 2, and 20. The sum of the $i_\perp$ and $i_\parallel$ terms (shown in grey) are included for the Rayleigh particle ($\alpha = 0.1$).

2.1.3. Efficiency parameters for intermediate sized paticles

For particles that have roughly the same diameter as the wavelength of light ($0.2 \leqslant \alpha \leqslant 10$) the electromagnetic field experienced by the particle is not uniform across the particle and solution of Maxwell’s equations must be pursued to adequately describe light scatter/absorption. For spherical particles, the familiar Mie solution can be pursued. For non-spherical particles (applies to dust) alternate methods are required as discussed in 2.2. In either case, the computations involved are complex. Fortunately, computer codes have been developed to provide rapid solutions. We direct the reader to the work of Dave (1968),Wilson and Reist (1994), or Bohren and Huffman (1983) for codes. Alternatively, versions of these codes (and others) are freely available on the world wide web (examples include: http://www.hiwater.org/; http://omlc.ogi.edu/software/mie/; http://www.ugr.es/~aquiran/codigos.htm; http://diogenes.iwt.uni-bremen.de/vt/laser/wriedt/Mie_Type_Codes/body_mie_type_codes.html; http://www.giss.nasa.gov/staff/mmishchenko/t_matrix.html). These codes often return the key variables used to describe light scattering and absorption by intermediate size range particles if particle refractive index, shape, and size parameters are known. In some instances, the properties of polydisperse aerosols can be considered. It is common to obtain single particle extinction, scattering, and absorption efficiencies (Q_{ext}, Q_{scat}, Q_{abs}) along with Mie intensity parameters ($i_\perp$ and $i_\parallel$) through use of these codes. The Q terms can be used to calculate a given particle's optical cross section as discussed previously. The Mie intensity parameters are useful for describing the angular directionality and resulting polarization of scattered light.

Fig. 4 provides an illustration of how Q_{scat} scales with particle size parameter for a spherical water droplet ($m = 1.33$). As observed, typical values for the Q terms for the intermediate size range are 0–5. At very small values of α, the Mie theory is effectively reduced to the Rayleigh regime described earlier where Q_{scat} scales with d^4. After passing through a maximum value, Q then tends to oscillate around a limiting value of 2 at large size parameters. This is typical of scattering that can be treated through the geometric optics approach to be discussed shortly. This figure was generated from theory for a spherical particle of specific size and refractive index probed with a monochromatic beam. The complex pattern of oscillations observed in the figure tend to be smoothed significantly when considering a polydisperse aerosol or for particles with irregular shape.

2.1.4. Mie intensity parameters and angular dependence of Mie scatter for spheres

If a Mie size range sphere is illuminated with unpolarized light of intensity I_0 and wavelength λ then the scattered intensity at a distance R and scatter angle θ is:

$$I(\theta) = \frac{I_0\lambda^2(i_\perp + i_\parallel)}{8\pi^2R^2} \tag{15}$$

The $i_\perp$ term describes the intensity of scattered light at a particular angle with polarization perpendicular to the scatter plane. Alternatively, the $i_\parallel$ term describes the intensity of scattered light at a particular angle with polarization parallel to the scatter plane.

Note the total scatter intensity is related to the sum of the two polarization components. Unlike Rayleigh scatter, the intensity of Mie scatter exhibits a strong angular dependence with scatter in the forward lobe near 0° often dominating. Plots of Mie intensity parameters as a function of scattering angle are often used to visualize the angular dependence of Mie scatter. Such a plot is illustrated in Fig. 3 for a water droplet of varying size parameter. Notice that as particle size parameter increases the absolute amount of light scattered (related to area under each curve) also increases. Furthermore, the Mie intensity parameters at very small angles are typically larger (notice logarithmic y-scale) than those encountered at larger scattering angles. This situation often complicates measurement of light scattering or extinction as it is experimentally difficult to collect or remove light scattered very near 0°. However, if the angular distribution and/or polarization of scattered light from a particle is determined, this data can be used to obtain information about particle size and/or refractive index.

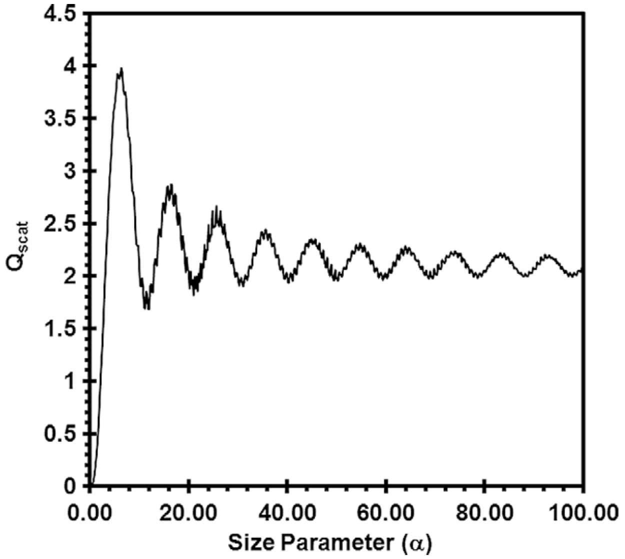

Fig. 4. Single particle scattering efficiency parameter plotted as a function of size parameter for a water droplet ($m = 1.33$). Since this particle was treated as a non-absorbing sphere $Q_{scat} = Q_{ext}$.

Two useful parameters for describing the hemispheric inequity (forward vs. back scatter) of the scattered light for Mie size range (and larger) particles are the asymmetry parameter (g) and the hemispheric backscatter ratio (b). The asymmetry parameter is the intensity weighted average of the cosine of the scattering angle.

$$g = \frac{1}{2}\int_0^\pi \cos\theta P(\theta)\sin\theta\, d\theta \tag{16}$$

where $P(\theta)$ is the phase function (angular distribution of scat. light). The value of g ranges from -1 to +1, it will be positive if forward scatter is dominant, and take a negative value if backscatter is dominant. The asymmetry parameter equals 0 when scattering is symmetrical about 90°. The hemispheric backscatter ratio (b) is the fraction of the scattered intensity that is directed in the backward hemisphere of the scattering coordinate system (90–180°). The backscatter ratio can be measured directly using certain commercially available nephelometers.

2.1.5. Geometric optics regime

When the dimensions of a scattering particle is very large compared to the probe wavelength ($\alpha > 10$) scattering behavior can be adequately explained by the laws of reflection, refraction, diffraction, and transmission at the particle air interface and within the particle itself. This treatment is of course complicated by the geometry of the particle with respect to the incident beam.

For these particles the single particle scattering efficiency parameter Q_{scat} can be modeled as a sum of three terms, each describing a particular optical effect:

$$Q_{scat} = Q_{diff} + Q_{refl} + Q_{tr} \tag{17}$$

In this equation Q_{diff} describes the efficiency of diffraction, Q_{refl} describes the reflection efficiency for the light initially incident on the particle, and Q_{tr} is the efficiency for transmission of light for 1 or more passes through the particle. The diffraction efficiency Q_{diff} for these particles is assumed to be 1. The extent to which the incident beam is reflected (reflection efficiency) depends on the refractive index of the particle and medium, angle of incidence, and polarization of the probe beam. The efficiency of transmission of light through the particle is complicated by the fact that after entering the particle the ray can be internally reflected one or more times. Thus, the transmission efficiency is treated as the sum of a series of reflections:

$$Q_{tr} = Q_{tr1} + Q_{tr2} + Q_{tr3} \cdots = \sum_{j=1}^{\infty} Q_{tr,j} \tag{18}$$

In this equation $Q_{tr,j}$ represents the contribution from a ray that has undergone $j-1$ reflections off the particle/air interface. It is interesting to compare the quantities of light reflected and transmitted via this type of treatment. Bohren and Huffman (1983) have provided such a comparison. For a large, non-absorbing sphere of $m = 1.33$ (water droplet) a Q_{refl} of 0.06593 is reported for visible wavelengths. This is in contrast to a Q value of 0.8845 for the light transmitted after a single pass through the particle. Excluding the effects of diffraction, much more light is dispersed after transmission through the particle compared to initial reflection. An interesting phenomenon occurs for non-absorbing particles if subsequent internal reflections are considered. When all internal reflections are considered, ($Q_{refl} + Q_{tr}$) approaches a value of 1 and all the light incident on the particle is accounted for. Since Q_{diff} is also assigned a value of 1, we can see that Q_{scat} approaches a limiting value of 2. This phenomenon is observed in Fig. 4, where at large values of α the extinction efficiency parameter for a non-absorbing particle is found to oscillate around the limiting value of 2.

For a light absorbing particle we would expect the Q_{tr} term to become smaller since light can be absorbed during transit through the particle. For a sufficiently large particle or sufficiently strong absorber, the Q_{tr} term would be expected to approach 0 and consequently Q_{abs} should approach $1 - Q_{refl}$. For weakly absorbing spheres, when the condition $4\alpha k \leqslant 1$ can be met, Bohren and Huffman (1983) suggest the absorption efficiency parameter can be given as:

$$Q_{abs} = \frac{8k\alpha}{3n}\left[n^3 - (n^2 - 1)^{\frac{3}{2}}\right] \tag{19}$$

This equation may yield results similar to those obtained through more formal calculations for weakly absorbing wind-blown dust.

2.2. Optical effects of non-spherical particles

While Mie theory provides solutions for light scattering by spheres, many particles in the atmosphere are non-spherical. Mineral dusts are no exception and feature complex morphologies with variable composition, particle size, and irregular shape distribution as reflected in Fig. 5a. Modeling individual dust particles as simple spheres of uniform refractive index may introduce significant error in the analysis. This is demonstrated by Fig. 5b which illustrates a plot of the single particle extinction efficiency parameter (Q_{ext}) as a function of particle size parameter (α) for a sphere, spheroid (particle B), and two additional shapes for $m = 1.52 + 0.0043i$. This example is particularly interesting since both the real and imaginary portion of the refractive index used in this example are fairly close to that encountered for mineral dusts. For calculation of size parameter for the non-spherical particles, the radius of a sphere with equivalent projected area was considered. As illustrated, shape can alter the maximal Q_{ext} value by roughly 25% and shift the particle size associated with this maximum considerably. The effect of nonsphericity on polarization state of scattered light can often be even more dramatic (Gogoi et al., 2009).

Microscopic features (cracks, surface roughness, inclusions of differing mineralogy etc...) on the order of the wavelength of light make modeling the optical properties of mineral dusts even more challenging. The particle surface itself can be rough, and other small particles may agglomerate on the surface to effectively add surface roughness. As such, no computational model has yet been demonstrated that can adequately account for all effects. However, the measurement and theoretical treatment of light scattering by non-spherical particles continues to be of intense scientific interest. This is reflected in the multiple texts on the topic that have been authored in recent years (Mishchenko et al., 2000; Wriedt, 1999; Taflove and Hagness, 2000; Doicu et al., 2000; Li et al., 2002; Jin, 2002; Mishchenko et al., 2002; Babenko et al., 2003; Doicu et al., 2006; Borghese et al., 2007). We would also direct the reader to a series of recent special issues of the *Journal of Quantitative Spectroscopy and Radiative Transfer* devoted to reporting on the proceedings of the annual Conference on Electromagnetic Scattering by Non-Spherical Particles (for instance JQSRT vol. 100(1–3), 1–496; JQSRT, vol. 106, 1–621; JQSRT vol. 109(8), 1335–1548; JQSRT vol. 110(14–16), 1207–1780, 2009). These volumes are particularly useful to track developments in the field as they evolve. Our consideration of the optical effects of non-spherical particles will be limited to brief discussions of computational techniques commonly employed. Detailed discussion of the computations involved is well beyond the intent of this work. Fortunately, a substantial number of printed pages have already been devoted to such pursuits and we direct interested readers to these works whenever possible in the paragraphs that follow. At present, there are several common alternatives for computational treatment of non spherical particles they are (1) the Discrete Dipole Approximation (DDA), (2) Finite Difference Time Domain (FDTD) method, and (3) the T-matrix method.

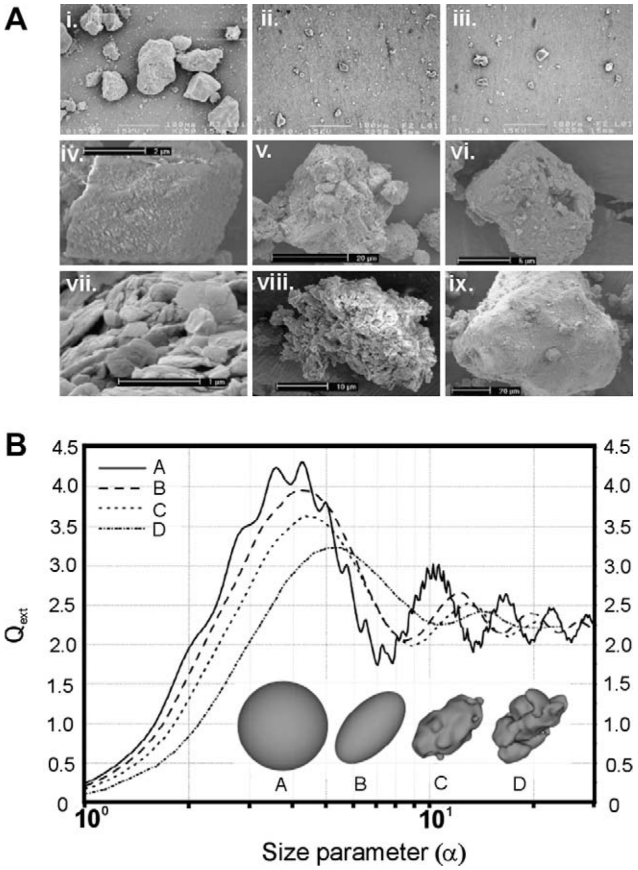

Fig. 5. (A) SEM images of dusts and soils. Image i and iv–ix are Saharan mineral dust particles from a soil sample. Image *ii* is red clay from France, and image iii is loess from Hungary. Notice the irregular, non-spherical appearance of all particles. Images i–iii are reproduced from http://www.astro.uva.nl/scatter/ with permission of author. Images iv–ix. Reproduced from Nousiainen (2009) with permission. (B) Plot of single particle extinction efficiency parameter (Q_{ext}) vs. particle size parameter (α) for a sphere, spheroid, and other shapes ($m = 1.52 + 0.0043i$) as calculated with the discrete dipole approximation approach of Yurkin et al. (2007b). Figure reproduced from Gasteiger et al. (2009) with permission of authors. (For interpretation of the references to color in this figure legend, the reader is referred to the web version of this article.)

2.2.1. Discrete dipole approximation

The discrete dipole approximation (DDA) method is one approach to modeling optical properties of arbitrary, inhomogenous particles. The model was originally proposed by Purcell and Pennypacker (1973), and has recently been reviewed by Yurkin and Hoekstra (2007a) and is considered by Draine in Chapter 5 of "Light Scattering by Nonspherical Particles: Theory, Measurements, and Applications" (Mishchenko, Hovenier, and Travis eds.). The general approach employed in DDA is the particle is treated as a large number (N) of point dipoles which can interact with each other (thus sometimes called coupled dipole) and the incident electromagnetic field. In turn, this yields N equations which are solved to yield dipole polarizations, and through this process both angular and integrated particle optical properties are obtained.

The major advantage of DDA is its ability to consider irregular particle shapes. It is only limited by the practical consideration of computational power. Additionally, several DDA codes are publicly available (SIRRI, DDSCAT is available at http://www.astro.princeton.edu/~draine/DDSCAT.html; ADDA at http://www.science.uva.nl/research/scs/Software/adda/). The relative merits of these codes have been discussed by Penttila et al. (2007). The freely available and widely used DDSCAT allows generation of dipole arrays for ellipsoids, rectangular and hexagonal prisms, tetrahedra, and user-supplied geometries. The numerical accuracy of the DDA method is often tested by considering the spherical geometry for which Mie solutions are available for reference. In many instances, DDA provides solutions within a few percent of the Mie value, if an adequate number of dipoles are used in the analysis.

A present limitation to the DDA method is the fact that required computational time/resources scale nonlinearly with both particle size (as number of dipoles increase) and refractive index of the medium. This is particularly problematic for large particles. For instance, Yurkin et al. (2007b) have explored the DDA method for spherical particles with size parameters >10 through using 64 Intel 3.4 GHz processors in parallel for the computations. They considered between 2.6×10^5 and 1.3×10^8 individual dipoles per computational grid. For particles of $\alpha = 20$, computations required >500 s for particles with refractive indices typical of mineral dusts. For larger particles and refractive index, computational times can be measured in units of days or weeks.

2.2.2. Finite difference time domain (FDTD) method

The origin of the FDTD method has been attributed to the work of Yee (1966). A detailed description of the method can be found in Chapter 7 of "Light Scattering by Nonspherical Particles: Theory, Measurements, and Applications" (Mishchenko, Hovenier, and Travis eds.) and the text by Taflove (2000). Several FDTD codes (and other types) are available at the website entitled "Electromagnetic Scattering Codes" maintained by Thomas Wriedt of the University of Bremen (http://diogenes.iwt.uni-bremen.de/vt/laser/wriedt/index_ie.html).

The FDTD method can be used to model the interaction of electromagnetic radiation with scatterers of complex geometry and inhomogenous composition. In this technique space is broken into small grid boxes and a scattering particle embedded in the coordinate system. Each box is assigned descriptive numerical values based on its permittivity, permeability, and conductivity – thus irregular particles and inclusions can be described. The FDTV approach then seeks solutions to Maxwell's equations in the time domain rather than frequency domain. That is, the evolution of fields are tracked step-wise in time for some small δt. At $t = 0$ a plane wave is generated and then propagated toward the particle in subsequent time steps. Eventually, the wave interacts with the particle and the incident radiation field altered. Clearly, the area defined by the grid space cannot be infinite in a computational model, so an artificial boundary must be imposed. The boundary itself must be either transmittive or absorbing such that reflections off the artificial boundary walls do not interfere in the analysis. The time-domain data recorded through the time steps is then transformed into the frequency domain, and the near-field data transformed into far-field scattering properties.

The individual grid box elements must be small compared to the size of the scattering particle and the wavelength of light considered. At optical wavelengths, this necessitates a large number of grid points. Both the required computational memory and processing time increase with the number of spatial grid points. As such, FDTD computations can also be quite time consuming. This limits use of FDTD to particles with size parameters less than about 10 (Mishchenko et al., 2000). However, the FDTD technique has several advantages including it can easily consider impulse response since it is a time-domain technique. The time domain data is also very useful to create animations that visually describe the propagation of the waves in both space and time.

2.2.3. T-matrix method

The so-called T-matrix approach is a computationally efficient and widely used method for computing light scattering of nonspherical, rotationally symmetric particles such as spheroids, cylinders, clusters of spheres, or Chebyshev particles. The method was originally introduced by Waterman (1965, 1971). The topic has been reviewed by Mishchenko et al. (1996) and has been the focus of several book chapters (for instance Chapter 6 of text edited by Mishchenko, Hovenier, and Travis or Chapter 5 of the text by Liou, 2002) and numerous recent scholarly articles (Mishchenko et al., 2007; Mishchenko et al., 2008).

While the aforementioned works provide a much more extensive consideration of the computational approach involved, the basic idea involves expanding the incident and scattered fields for a plane wave scattered by a particle in vector spherical wavefunctions (VSWFs). This process introduces terms known as expansion coefficients often given the symbols a, b and p, q for the incident and scattered wave, respectively. Since Maxwell's equations and boundary conditions used are linear, so must be the relationship between the expansion coefficients for the incident and scattered wave. The expansion coefficients can then be related via a transition matrix (T-matrix):

$$\begin{bmatrix} p \\ q \end{bmatrix} = \mathrm{T} \begin{bmatrix} a \\ b \end{bmatrix} \tag{20}$$

If the T-matrix for a scattering particle can be determined, the expansion coefficients can be related and the scattered field described. A major advantage of this approach is the T-matrix itself depends only on the particle (shape, orientation, size, composition) and is independent of the incident wave. So for a particular particle the T-matrix only needs to be determined once, and can be used in subsequent calculations which makes the approach efficient for multiple calculations.

The only problem which remains is solving for the T-matrix itself. This is often accomplished by the extended boundary condition method (EBCM) of Waterman (1971). This restricts the particles considered to be homogenous and isotropic but provides an efficient method, particularly if the particle has an axis of symmetry (Nieminen et al., 2003). Alternate methods may also be employed to yield the T-matrix if EBCM is unacceptable. Nieminen et al. (2003) has suggested the FDTD method could be used, Mackowski (2002) has demonstrated use of the DDA method, and a point matching method has been discussed by Nieminen et al. (2003). Fortunately, computer codes are publicly available to calculate scatter properties via the T-matrix method for particles with size parameters that can even exceed 100 (http://www.giss.nasa.gov/staff/mmishchenko/t_matrix.html).

3. Light scattering, absorption, and extinction by collections of particles in the atmosphere

3.1. Attenuation of a light beam by airborne particles

The attenuation of a beam of collimated, monochromatic light by a collection of particles in the atmosphere is often modeled by the Beer–Lambert law:

$$I_z = I_0 e^{-(b_{ext} z)} \tag{21}$$

where I_z is the light intensity at point z, I_0 is the initial intensity (e.g. when $z = 0$), b_{ext} is the aerosol extinction coefficient of the medium (m^{-1}), and z is the path length through the medium (m). This treatment assumes particles are evenly dispersed throughout the path, particles do not interact, and are spaced with enough distance (dilute) to assure only single scattering occurs. The extinction coefficient is sometimes referred to as the turbidity of the sample. The unit less product ($b_{ext}z$) can be referred to as the optical depth of the aerosol, although use of this terminology in the literature often implies a path through a vertical column of the atmosphere. It is clear the transmission of light (I_z/I_0) is a function of both distance traveled by the beam and the extinction coefficient of the aerosol. The extinction coefficient describes optical loss per unit distance. Near earth's surface values for $b_{ext} < 100\ Mm^{-1}$ are typical of the atmosphere on clear days, however much higher values are observed during fogs, dust storms etc...

For particles in the atmosphere, light extinction is caused by the cumulative effects of light absorption and scattering and we can write:

$$b_{ext} = b_{scat} + b_{abs} \tag{22}$$

where b_{scat} and b_{abs} represent the scattering and absorption coefficients (m^{-1}) for the aerosol. Thus, the effects of absorption and scattering are treated as if they are additive. Before proceeding, it should be noted that atmospheric gases also absorb and scatter light. For the purposes of this paper, we will discuss only the optical effects of aerosols so all values and discussions of scattering/absorption/extinction coefficients refer only to the effects of airborne particles.

3.2. Modeling the optical effects of monodisperse aerosols

Both the scattering and absorption coefficients of an aerosol are a function of the size, composition, and number density (concentration) of the constituent aerosol particles. For a monodisperse aerosol (single particle size) the scattering and absorption coefficients can be described as:

$$b_{scat} = \sigma_{scat}N = \pi r^2 Q_{scat}N \tag{23}$$

$$b_{abs} = \sigma_{abs}N = \pi r^2 Q_{abs}N \tag{24}$$

where N is the number concentration of particles (# particles/m^3). This model essentially sums up the effect of each particle in a sample while assuming it behaves independently from others. Simply scaling up the treatment of individual particles is conceptually simple. Unfortunately, it is not very common that particles in the atmosphere are all the same size (monodisperse).

3.3. Modeling the optical effects of polydisperse aerosols

When the size distribution $N(d)$ of the aerosol is known or can be suitably modeled by a size distribution function such as a power-law or log-normal distribution, and all particles have the same refractive index, the extinction coefficient of the sample can be found by integrating over the particle size distribution:

$$b_{ext} = \int_0^{d_\infty} \frac{\pi D^2}{4}\ Q_{ext}N(d)\ dD \tag{25}$$

In practice, this would be accomplished by breaking the size distribution into narrow bins of width ΔD and summing the contribution of each bin. Scattering or absorption coefficients can be found by an analogous approach in which Q_{scat} or Q_{abs} is substituted for Q_{ext}. Externally mixed aerosols (particles of different compositions present in same volume but not same particles) present the problem of multiple refractive indices. In this case, the effects of each particle type can be considered individually, and the sum of all particle types then computed. Internally mixed aerosols (multiple components within a given particle) present an even greater challenge for modeling due to small variations in the specific microphysical properties of the particle under study. Nonetheless, the problem is often attacked through using "mixing rules" such as the Bruggeman effective medium approximation (Bohren and Huffman, 1983).

3.4. Reconstruction of light extinction through aerosol composition data

An alternate, more practical approach to estimating aerosol scattering, absorption, and extinction coefficients in the atmosphere is to reconstruct these parameters from aerosol composition data (if available). This approach has been considered extensively by the Interagency Monitoring of Protected Visual Environments (IMPROVE) program (http://vista.cira.colostate.edu/improve/). The basic idea is to scale specific optical effects such as extinction or scattering coefficient with mass concentration of a particular component of the aerosol ($NH_4(SO_4)_2$, NH_4NO_3, organic carbon, elemental carbon, wind blown dust, etc...) and then sum the effects of all components. Mathematically, we can write:

$$\begin{aligned} b_{ext} &= E_{ext\,comp.1}M_{comp\,1} + E_{ext\,comp.2}M_{comp\,2} + E_{ext\,comp.3}M_{comp\,3} + \cdots \\ &= \sum_{n=1}^{i} E_i M_i \end{aligned} \tag{26}$$

where the E terms represent mass extinction coefficients (m^2/g) for each component of the aerosol and the M terms represent mass concentrations. Corrections for ambient relative humidity should also be employed since the optical properties of atmospheric aerosol are known to change with humidity. While this approach completely overlooks the mixing state of the aerosol, studies have shown that mass scatter coefficients for models of internally and externally mixed aerosols often differ by <10% (Malm and Kreidenweis, 1997; Malm et al., 1997; Lowenthal et al., 2000; Sloane and Wolff, 1985; Sloane, 1983; Sloane, 1984). Typical values for mass scatter coefficients in the mid-visible are in the range of 3–4 m^2/g for the fine mode inorganics and organic carbon and typically 0.5–1 m^2/g for soils and larger coarse mode particles. It should be noted that mass extinction coefficients vary considerably with particle size as illustrated in Fig. 6. This figure represents a plot of mass extinction coefficient vs. size parameter for a spherical water droplet. The most efficient scatterers on a per mass basis are generally particles with diameters slightly less than 1 micrometer. Larger particles typical of wind blown dusts scatter light less efficiently. However these particles often can contribute significantly to light extinction, particularly during dust storm events when dust mass concentrations can exceed 1 mg/m^3. The variability of mass extinction coefficient (E) with particle diameter illustrated in Fig. 6 also underscores the potential difficulties associated with direct conversions between aerosol mass loadings and optical properties.

3.5. Wavelength dependence of scatter/absorption

While the scattering and extinction behavior of a single particle can be modeled, it may be more useful to describe the wavelength dependence of scatter/absorption/extinction empirically. This could of course be accomplished by recording measurements of the aerosol's optical properties at various wavelengths. If this is accomplished, the data can often be fit to a power law such as:

$$b_{ext} = \beta\lambda^{-\alpha} \tag{27}$$

where β is the Angstrom turbidity coefficient and α is known as the Angstrom exponent. It is also common to see this type of equation written in terms of optical depth rather than extinction coefficient

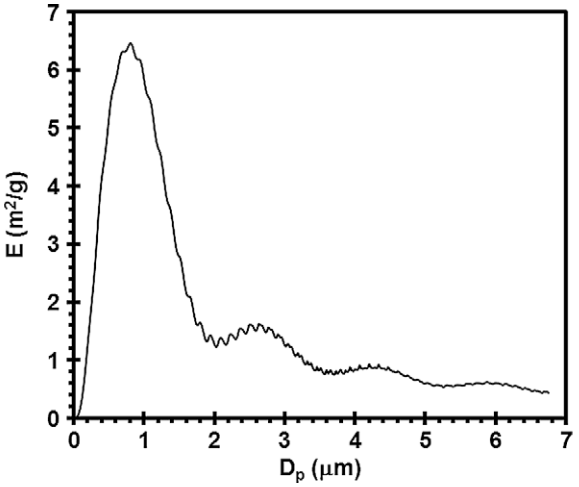

Fig. 6. Single particle mass extinction coefficients (E) plotted as a function of diameter for a unit density sphere with $m = 1.33$ and a probe wavelength of 530 nm. For this example, particles near 1 µm are the most efficient scatterers on a per mass basis. Plot was generated by the authors using MiePlot.

in which case the value of β would differ. The Angstrom exponent varies with particle size. It is typically larger for smaller particles (recall scatter by Rayleigh particles scale with λ^{-4}). The Angstrom exponent often varies between 0.5 and 2.5 for typical atmospheric aerosols, however, for coarse wind-blown dust α is usually less than 0.5. Absorption by aerosols is often modeled in a similar manner, however, the value of the exponent and pre-exponential term would correspondingly be different since it describes only the effects of absorption. Absorption Angstrom exponents for wind-blown dusts are often >3 in the visible region since the main light absorbing component in dust (hematite) absorbs light much stronger at short wavelengths (Schladitz et al., 2009).

3.6. Model for airborne dusts

As previously outlined in Section 2.2, the computational modeling of the optical effects of irregular, non-spherical particles can be challenging. A potential silver lining is the effects of ensemble averaging of non-spherical particles. Similar to the case for spheres, distributions of particle size, shape, material compositions, and roughness tend to smooth the signatures of the scattering properties of individual particles. Furthermore, a collection of large numbers of randomly orientated particles reduces the effective asymmetry of the ensemble with respect to shape/particle orientation. These effects reduce a massively complex collection of scattering entities into one which can be more effectively modeled. This phenomenon is best reflected by considering scattering matrices originally reported by Volten et al. (2001) and Muñoz et al. (2001) and discussed in Nousiainen's recent review on modeling optical properties of dust (2009). The scattering matrix relates the Stokes parameters of the incident radiation to that of the scattered radiation for each scatter angle (θ). If it is assumed that all particles considered have a symmetry plane, or alternatively if each particle has its mirror image present in the sample, the 4×4 scattering matrix reduces to the following block diagonal structure:

$$\begin{bmatrix} I \\ Q \\ U \\ V \end{bmatrix}_{scat} \alpha \begin{bmatrix} P_{11}(\theta) & P_{12}(\theta) & 0 & 0 \\ P_{12}(\theta) & P_{22}(\theta) & 0 & 0 \\ 0 & 0 & P_{33}(\theta) & P_{34}(\theta) \\ 0 & 0 & -P_{34}(\theta) & P_{44}(\theta) \end{bmatrix} \times \begin{bmatrix} I \\ Q \\ U \\ V \end{bmatrix}_{incident} \tag{28}$$

where $P_{11}(\theta)$ is the scattering phase function and all other elements are smaller than it. As such, the additional elements of the scattering matrix are often normalized to $P_{11}(\theta)$. It is also common to normalize $P_{11}(\theta)$ to its value for a scatter angle of 30°. Additionally, the ratio $P_{12}(\theta)/P_{11}(\theta)$ describes the linear polarization of the scattered light for an unpolarized incident beam.

Data from Volten et al. (2001) and Muñoz et al. (2001) as reproduced in Nousiainen (2009) is illustrated in Fig. 7a. For samples of Feldspar, red clay, green clay, loess, and Saharan dust, plots of normalized scatter matrix elements vs. scatter angle exhibit similar shapes. This is remarkable considering the wide array of material compositions, shapes, and effective diameters of the particles used in the study. While curves of similar shape are observed, resultant phase functions and polarization are still very different from that expected for spheres. Interestingly, this can be reconciled to a large extent for particles of similar size to the wavelength of light by modeling dust shape as spheroidal. The spheroid shape is defined by rotating an ellipse about either its minor (oblate) or major (prolate) axis (see Fig. 5b particle B). The spheroid is defined by two parameters: the radius of the volume equivalent sphere, and the ratio of its axis'. While it is clear from the SEM images in Fig. 5a that most dust particles are not true spheroids, the appeal of this model particle shape is solely found in how well it matches empirical data despite it not being physically accurate. Consider Fig. 7b as reproduced from Dubovik et al. (2006). This figure illustrates a plot of measured scattering matrix ratios (data points) vs. scattering angle for a Feldspar dust sample at $\lambda = 633$ nm. The plot also contains modeled values assuming spherical and spheroidal geometries for comparison (solid lines). As can be observed, treating the dust particles as spheres leads to large deviations from experimental data. However, the spheroidal model achieves a much better fit to observable data – particularly for the phase function and linear polarization. As such, the spheroid model for dusts is often used, and this model is currently employed in remote sensing applications such as AERONET and in retrievals from the MODIS platform (Feng et al., 2009; Dubovik et al., 2002a).

4. Measurement techniques for the study of the optical properties of airborne particles

A wide variety of methods have been developed to measure the optical properties of airborne particles. To a certain extent these techniques can be categorized as either point measurements, or techniques in which measurements are made over a large spatial area/path. The point measurements generally allow very precise study of the key optical properties of aerosols. However, by their very nature they suffer from not being able to see the "*big picture*." That is, point measurements generally are not able to provide horizontally and vertically resolved measurements of aerosols in both space and time. Instruments for point measurements can be installed on aircraft which helps solve this problem to an extent, but the expense involved in such airborne measurements makes this impractical for many investigations. On the other hand, for techniques which have the ability to quickly make measurements over a large spatial area/path the values of aerosol optical properties tend to be averages over the measurement path. This can make de-convolution of the effects of different aerosol types difficult. Therefore, many of the point and long-range techniques we will discuss truly are complimentary. In Sections 4.1–4.3, we provide a brief review of technologies available for measurement of aerosol optical properties. We omit a discussion of satellite remote sensing since this topic was recently reviewed by Martin (2008).

4.1. Point measurements of aerosol extinction coefficient

4.1.1. Transmissometer

The transmissometer is used to measure the extinction coefficient (b_{ext}) of aerosols, typically over long path lengths of

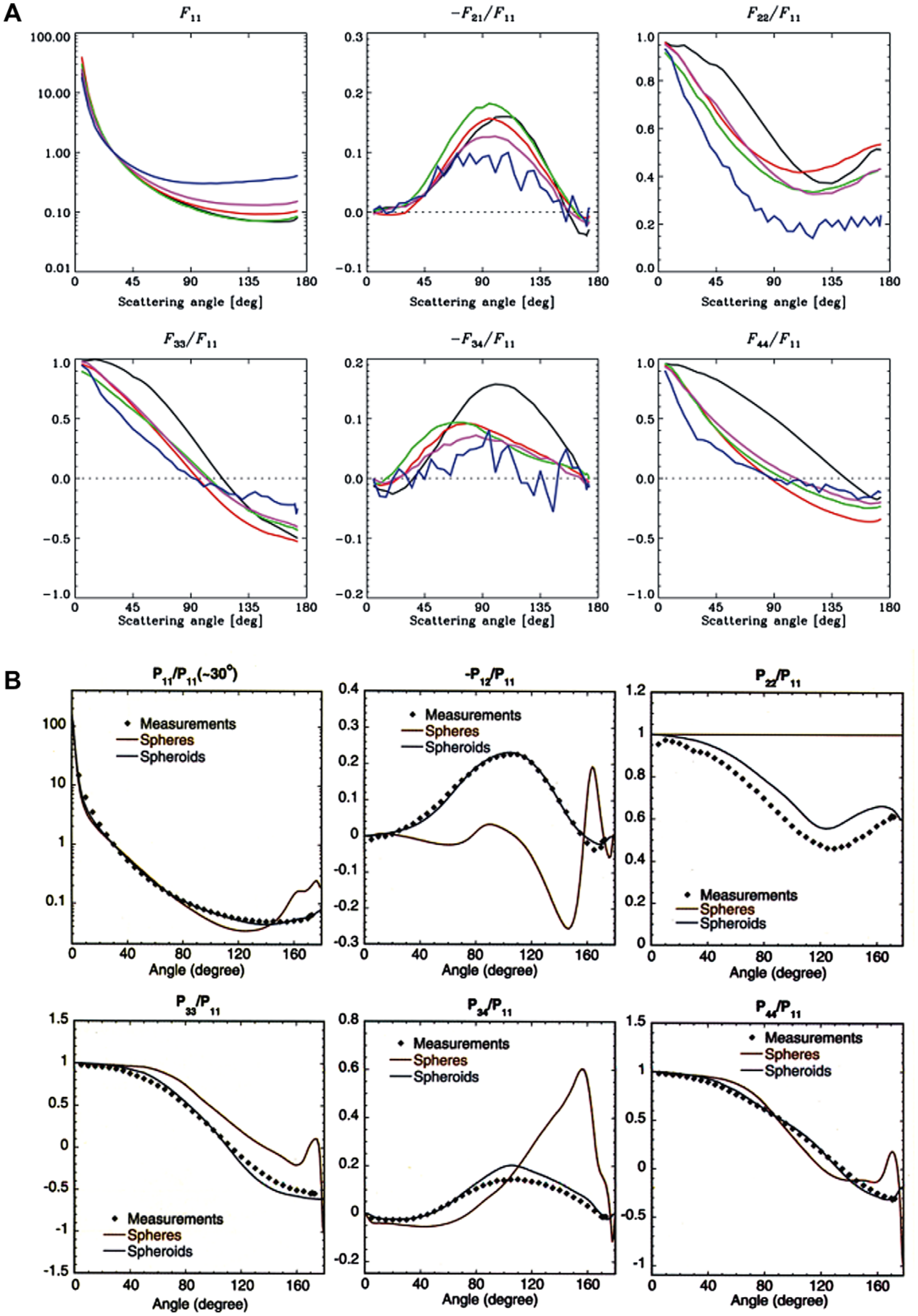

Fig. 7. (A) Plots of scatter matrix elements vs. scatter angle for Feldspar (black), Red clay (red), Green Clay (green), Loess (magenta), and Saharan dust (blue). Figure reproduced from Nousiainen (2009) with permission. Original data from Volten et al. (2001) and Muñoz et al. (2001). (B) Plots of measured scatter matrix elements (633 nm) vs. scatter angle for a Feldspar dust sample. This sample was chosen as a dust mimic. Also included are simulated plots assuming spherical and spheroidal particles. The spheroidal model is particularly effective at matching measurements for the phase function (P_{11}/P_{11}) and linear polarization (P_{12}/P_{11}). (For interpretation of the references to color in this figure legend, the reader is referred to the web version of this article.)

1–30 km. Given the long paths involved, the reader may wonder why we have termed this a "point" technique. We have done so since transmissometers are generally installed at a particular location rather than being mobile so extinction data is returned for a certain well-defined optical path. Fig. 8a illustrates an optimal implementation of the device. As illustrated, the instrument typically consists of two separate sections, a transmitter and a receiver spaced at some fixed distance. Aerosols present between the transmitter and receiver unit can scatter and absorb light, reducing the irradiance at the receiver in accordance with the Beer-Lambert law of attenuation. Optec, Inc. produces the Model LPV-3, which operates at 550 nm in either continuous or timed mode (Optec, 2005). The transmitter section consists of a lamp, projection optics, and a 4-bladed chopper for beam modulation. The chopper modulates the light at a rate of 78.125 Hz and an optical feedback circuit is used to maintain the lamp output constant to 1%. The receiver measures the difference between the irradiance levels when the transmitter is off compared to on, which minimizes the effect of background or ambient illumination (Malm and Persha, 1991). The receiver unit consists of a refractor lens, a silicon photodiode detector, and a computer. A 0.07° solid angle is defined to be the detector field of view, in order to reduce the effect of atmospheric optical turbulence (Molenar et al., 1989a). Optical turbulence causes beam spreading in path lengths greater than 2 or 3 km; this is interpreted by the detector as increased atmospheric extinction. The small field of view for the detector minimizes this error because it allows the detector to be focused on a uniform portion of signal, even when optical turbulence is present. The transmissometer must be placed so that the line of sight between transmitter and receiver remain clear and unobstructed (Molenar et al., 1989b). Even if the beam path is unimpeded, the beam can be distorted or reflected if passing too close to the surface. The Optec transmissometer offers a range of measureable extinction coefficients from 10 Mm^{-1} to 6.55 km^{-1} with a resolution of 0.1 Mm^{-1}. Both the transmitter and receiver can be placed in protective housings for long term, unattended operation.

4.1.2. Extinction cells

A shorter path-length analog to the transmissometer can be found in the form of extinction cells (see Fig. 8b). These devices pass a beam of light of varying wavelength through a tube filled with sample. The light is then incident upon a detector element and optical losses measured relative to a filtered air blank. This idea is conceptually very simple, and the method can be considered an absolute measurement if provisions are made to remove forward scattered light from reaching the detector. Indeed, the approach has been used as an accepted reference method in several comparison studies (Bond et al., 1999; Reid et al., 1998). However, measuring very small optical losses typical of atmospheric aerosol samples (<100 Mm^{-1}) can be experimentally challenging. Attempts to circumvent this usually involve increased sample path length. For instance, a 6.4 m long path was used by Weiss and Hobbs (1992) to measure the extinction coefficient at 538 nm of smoke plumes from Kuwaiti oil fires. The limit of detection in this study was approx. 20 Mm^{-1}, a rather impressive technical feat since this corresponds to a loss of only 20 ppm over a 1 m path! More recently, Virkkula et al. (2005) constructed a folded path extinction cell capable of measurement at 467, 530, and 660 nm. The effective path length was roughly 6.6 m and use of low-power LED technology and photodiode detectors make the approach efficient from both a power and cost point of view. Detection limits of ≈5 Mm^{-1} were reported for all three spectral channels. In general, this approach is particularly well-suited for measurements when relatively high mass loadings of particulates are present.

4.1.3. Cavity ring-down spectroscopy (CRDS)

An alternate technique for point measurement of aerosol extinction coefficient that has gained popularity in recent years is cavity ring-down spectroscopy (Bulatov et al., 2002; Smith and Atkinson, 2001; Thompson et al., 2003; Thompson et al., 2002; Moosmüller et al., 2005; Butler et al., 2007; Miller and Orr-Ewing, 2007; Thompson et al., 2008; Strawa et al., 2003; Riziq et al., 2008; Lang-Yona et al., 2009)). Briefly, cavity ring down methods measure the time constant (τ) for the attenuation of a laser pulse after it is introduced into a stable optical resonator formed between two highly reflective ($R > 0.999$) mirrors (see Fig. 8c). The light intensity observed by a light detector displays an exponential decay in time after the laser pulse. The rate of decay is governed by the reflectivity of the mirrors used and extinction of light by the sample placed between the mirrors. The time constant (τ) is the time required for the light signal to decay to $1/e$ (about 37%) of its original value. This time constant (τ) can be related to the extinction coefficient of the sample placed between the mirrors by:

$$\tau = \frac{t_r}{2[(1-R) + b_{exttotal}L]} \tag{29}$$

where t_r is the round trip transit time for the beam, R is the mirror reflectivity, L is the cavity length, and $b_{exttotal}$ is the sample's total extinction coefficient. In this equation, $b_{exttotal}$ refers to the cumulative effects of Rayleigh scattering by gases, aerosol scattering, aerosol absorption, and gas-phase absorption. To measure the effects of only aerosols, it is necessary to subtract the effects of Rayleigh scattering losses and gas phase absorption from the total extinction measurement ($b_{exttotal}$) made with a CRDS system. This is often accomplished by measuring the ring-down time constant for the sample containing aerosol (τ_{sam}) and the ring-down constant for the cell filled with HEPA filtered ambient air (τ_{air}) and use of the following expression to extract aerosol extinction coefficient (b_{Ext}):

$$b_{ext} = \frac{1}{c}\left(\frac{1}{\tau_{sam}} - \frac{1}{\tau_{air}}\right) \tag{30}$$

CRDS based methods can achieve impressive sensitivity (b_{ext} det. lim. <1 Mm^{-1}) owing to the long effective path lengths (several km) involved. More importantly, the method is not affected by source intensity fluctuations since the rate of attenuation of light is the measured variable rather than absolute irradiance. This is very different than standard light transmission measurements. CRDS methods for aerosol detection have been demonstrated for numerous wavelengths in both the visible and near IR (see previously cited refs.).

4.2. Point measurements of aerosol scattering coefficient

Nephelometers are used to measure the scattering coefficient (b_{scat}) of aerosols at point locations. There are several nephelometer designs including the integrating nephelometer, reciprocal nephelometer, and polar nephelometer. Integrating nephelometers are available commercially (TSI Inc., Radiance Research, Ecotech, Optec Inc.) and are widely used in air quality monitoring.

4.2.1. Integrating nephelometer

Beuttell and Brewer (1949) invented the integrating nephelometer in 1949 as a method to measure visual range. A schematic of an integrating nephelometer is shown in Fig. 9a. The device attempts to measure light scattered by a sample of air over all angles (0–180° – hence the term "integrating"). In the device illustrated in the figure, an air sample containing particles is drawn into tube and illuminated with light from a flash lamp. The light from the lamp is passed through an opal glass diffuser in an effort to achieve a near Lambertian source. The sample (scattering) volume is

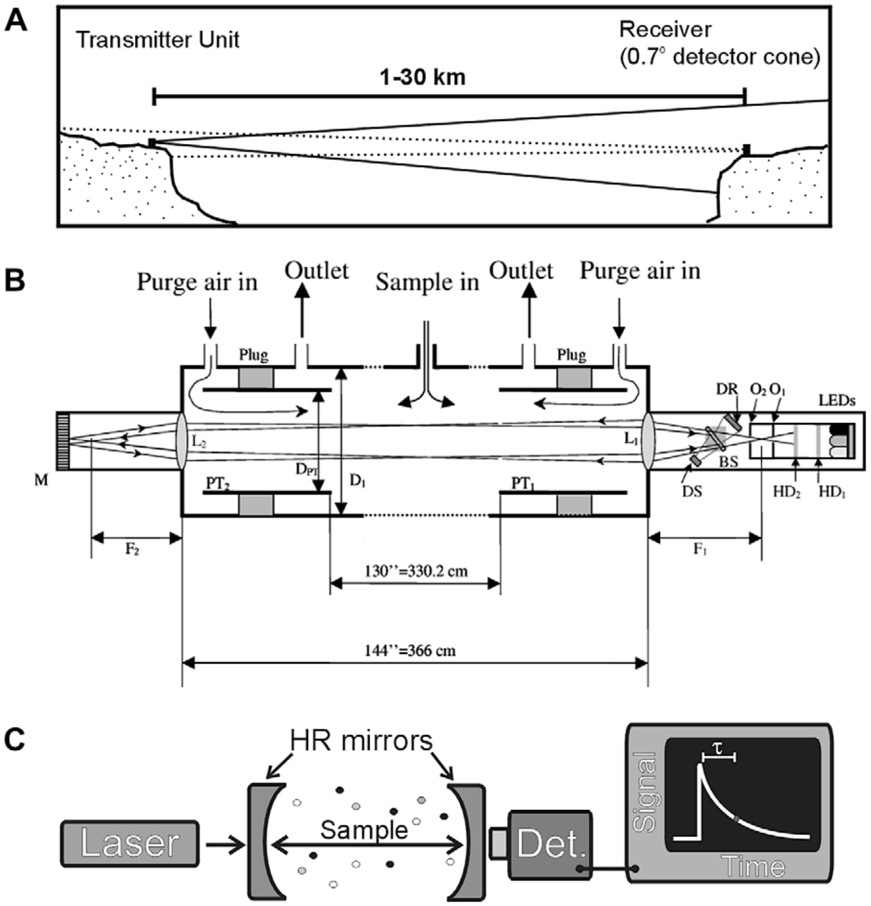

Fig. 8. Methods for determination of aerosol extinction coefficient (b_{ext}). (A) Implementation and optimal placement of transmitter and receiver units of a transmissometer. The transmission between the transmitter and detector unit is monitored and optical losses are assumed to be governed by Beer's law of extinction. (B) Extinction cell of Virkkula et al. (2005) (reproduced with permission of author). HD – holographic diffuser, O – orifice, DR – reference detector, DS – signal detector, L – lens, PT – purge air tube, M – mirror. (C) Typical apparatus for cavity ring-down spectroscopy (CRDS). In this technique light from a pulsed laser circulates between two highly reflective mirrors and the time constant for the exponential decay of light intensity measured. The aerosol sample is placed between the mirrors and the time constant τ related to extinction through Eqs. (29) or (30).

viewed by a suitable light detector such as a photomultiplier tube (PMT) through an optical filter to select a certain wavelength range and several small apertures to help minimize wall scatter. At the far end of the tube is a highly efficient light trap. This optical arrangement helps assure light which reaches the detector originates from a narrow cone containing the scattering sample. Now, if light is scattered from the right of the lamp in the figure towards the PMT this represents backscatter (90–180°). Alternatively, if scattered light originates from the left of the lamp in the tube this is forward scatter (0–90°). By illuminating the entire cone and using a tube of suitable length for the sample chamber, scattered light can most always be collected over ≈15 – 165°. However, real nephelometers invariably fall short of perfection due to geometric constraints and cannot collect scattered light very near the forward (0°) and reverse (180°) directions. This leads to defining of a truncation angle for a particular device that represents the angles from which light cannot be collected. While this may seem like a minor experimental issue, it is actually of significant consequence for making accurate measurements of scattering coefficient (b_{scat}). This results because particles do not scatter light isotropically, but rather scattering tends to be peaked at the small angles where it may not be collected. This can result in systematic underestimation of scattering coefficient known as truncation error. Fortunately, correction factors for angular non-idealities have been pursued to redeem measurements made with certain commercially available nephelometers (Anderson and Ogren, 1998; Heintzenberg et al., 2006). In principle, nephelometers can be constructed for measurements at any wavelength. TSI Inc. offers a three wavelength model with measurements made simultaneously at 450, 550, and 700 nm (40 nm bandwidth) so Angstrom exponent can be estimated from resultant data. The Radiance Research M903 nephelometer uses a filter to spectrally select green light (exact pass band depends on specific device). Ecotech offers a nephelometer for measurements at 450, 525, and 635 nm. Certain models are equipped with a retractable backscatter shutter that prevents light from being scattered in the forward direction. This allows measurement of backscatter fraction of the aerosol, and important variable related to aerosol climate forcing. In general, integrating nephelometers are capable of measuring particle scattering coefficients in a range from 0.3 $\mathrm{Mm^{-1}}$ to 10^{-2} $\mathrm{m^{-1}}$.

4.2.2. Integrating sphere (reciprocal) nephelometer

In the integrating nephelometer described in Section 4.2.1 a diffuser was used to provide a Lambertian illumination pattern and light was detected at a fixed point. An alternate approach to nephelometer design is the reciprocal nephelometer, in which a collimated beam is used and light is detected by a cosine detector. In recent years there have been several reports of such a device. Varma et al. (2003) have constructed an integrating sphere nephelometer in an effort to reduce the truncation error associated with conventional integrating nephelometers. In this instrument, an integrating sphere is used as the sample cell. The inner surface of

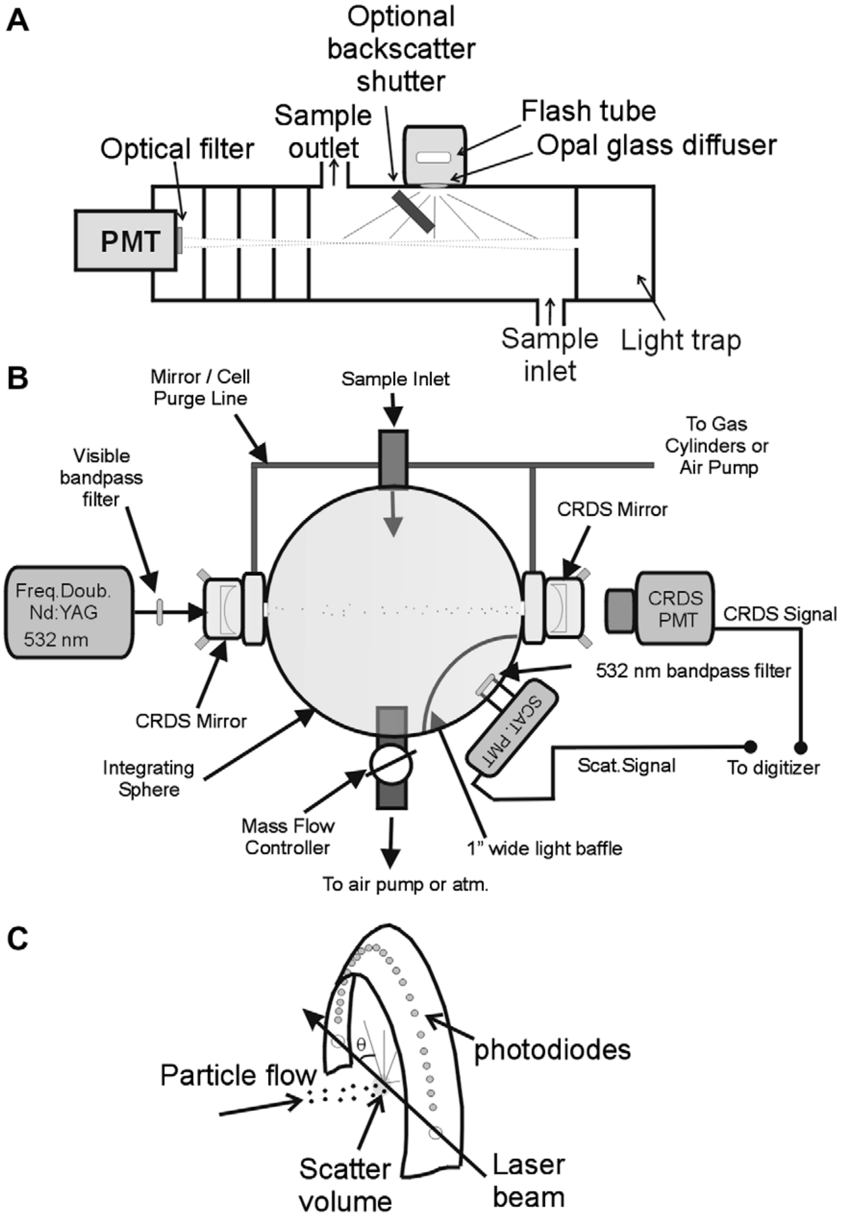

Fig. 9. (A) Illustration of an integrating nephelometer. The aerosol sample fills the measurement chamber and is illuminated by light passing through a diffuser. Forward scatter originates from particles to the left of the lamp, while backscatter originates from particles to the right of the lamp. The backscatter shutter is used to eliminate forward scatter is optional and retractable. It can be used to measure backscatter fraction. (B) Illustrates one type of integrating sphere nephelometer (adapted from Thompson et al., 2008 with permission of author). The sphere collects light scattered by aerosols residing in the probe beam volume. In this particular experiment cavity ring-down measurements were carried out to simultaneously determine both b_{ext} and b_{scat} . (C) Illustrates a typical polar nephelometer. In this device an array of photodiodes placed at a radius from the scatter volume can be used to probe the angular dependence of scatter. Typical devices may have 20–30 such photodiodes arranged between $\theta = 0–180°$.

the sphere is coated with a highly reflecting (>99%) barium sulfate based coating. The aerosol is probed by a laser beam from a frequency doubled Nd:YAG laser at 532 nm. Light scattered by the beam is collected by the sphere and directed to a photomultiplier for detection. The beam passes through two small apertures of 5 mm radius on each pole of the sphere, and truncation reduction tubes are attached yielding an instrument truncation angle of only about 1° for the device (in contrast to 7–15° for int. neph.). This reduces measurement error for large particles, which is particularly important for coarse mode dusts. Another advantage of the sphere design is nearly all scattered light is collected by the sphere, a condition which should affect detection limits favorably. A similar integrating sphere nephelometer was reported by Fukagawa et al. (2005) and an integrating sphere nephelometer reported by Thompson et al. (2008) is illustrated in Fig. 9b. In the latter method, the aerosol sample was simultaneously probed by ring down spectroscopy yielding extinction coefficient (b_{ext}) and correspondingly single scatter albedo. To the best of our knowledge, the integrating sphere design is not yet commercially available.

4.2.3. Polar nephelometer

The major difference between polar and integrating nephelometers is a polar nephelometer is designed to make measurements of the angular pattern of light scattered by the aerosol sample. Knowledge of the angular distribution of scattered light can provide significant clues to the aerosol sample such as asymmetry parameter, backscatter fraction, particle size, or refractive index. A polar nephelometer may have multiple detectors, which lie in a half circle around the sample flow path as shown in Fig. 9c (Barkey and Liou, 2001; Gayet et al., 1997; Barkey et al., 2007). Another possible orientation is to have one detector and a collimating lens on a moveable arm that is physically moved through a series of angles (Lienert et al., 2003). Photodiodes coupled to optical fibers are often used as detectors for the first style mentioned. To a certain degree the number of angles over which measurements can be made is limited by the desired complexity of the device. While polar nephelometers generally are not as sensitive as the instruments discussed in Sections 4.2.1 and 4.2.2 they can provide important details regarding the angular distribution of scattered light that conventional devices cannot.

4.3. Point measurements of aerosol absorption coefficent

Methods to measure and monitor aerosol absorption coefficient (b_{abs}) can be grouped into two classes: those based on filter sampling and those capable of *in situ* measurements. The particle soot absorption photometer (PSAP), and aethelometer are the most commonly used filter based techniques. The filter based techniques are conceptually simple, relatively inexpensive, insensitive to absorbing gases, and robust. However, they rely on collecting particles on a filter medium which can complicate measurements. The *in situ* techniques of photoacoustic spectroscopy and photothermal interferometry offer the advantage of probing the aerosol while it is still dispersed. Moosmüller et al., 2009) have also recently reviewed recent developments in the field of aerosol light absorption.

4.3.1. Particle soot absorption photometer (PSAP)

Fig. 10a illustrates a schematic of the PSAP instrument. The PSAP method is capable of providing real-time monitoring of aerosol absorption. Additionally, the PSAP has been subject to a number of studies aimed at evaluating its performance (Bond et al., 1999; Arnott et al., 2003; Sheridan et al., 2005). In this device, air containing particles is drawn through a filter at constant volumetric flow rate. The optical transmission of the filter is continually monitored through use of a light source and photodetector. A second filter is used for the reference (blank) measurement. This reference filter is placed in the air flow path immediately after the primary filter (primary filter removes particles). Use of the reference filter for blank measurements assures changes in source brightness over time are not measured as absorption. When particles deposit on the first filter, the filter transmission decreases, and less light reaches the detector. The derivative of the detector signal in time is measured and this quantity is proportional to the aerosol absorption coefficient. Based on this model, the apparent aerosol absorption coefficient (b'_{abs}) can be expressed as:

$$b'_{abs} = \frac{A}{V}\ln\left(\frac{I_0}{I}\right) \tag{31}$$

where A is the area of the spot on which particles are collected (m^2), V is the volume of air sampled (m^3) during the sampling period, and I_0 and I are the measured filter transmittances for the prior and current sampling period. At first glance the PSAP appears to be a fairly simple device, however, measurements can be complicated by the effects of multiple scattering of light off the fibers of the filter medium. This results in photons which traverse the filter having experienced a certain "effective" path length greater than the filter thickness. A significant problem arises since this effective path length decreases as the filter becomes more heavily loaded with particles in a non-linear way. This can lead to systematic error in measurement of b_{abs} if not corrected for. Fortunately, this is a well-known phenomenon and empirical corrections have been developed by the instrument manufacturer to account for this effect. The b_{abs} value reported by the PSAP is actually:

$$b_{abs} = \frac{b'_{abs}}{2(0.5398\tau + 0.355)} \tag{32}$$

where τ is the filter transmission (filters are generally changed when τ drops to 0.7). During use, the PSAP instrument will also register a measureable absorption even in the absence of an absorbing aerosol. This is because scattering by particles can also reduce the transmittance of the filter. Fortunately, this effect has been studied and a correction can be applied to the data collected. The correction factor which is often employed is 2% of sample scattering coefficient (b_{scat}) (Bond et al., 1999). Additionally, rapid changes in relative humidity can lead to measureable signals (so-called "wet T-shirt effect") (Schmid et al., 2006).

4.3.2. Aethalometer

Fig. 10b illustrates the optical chamber of an aethalometer. The aethalometer is very similar to the particle soot absorption photometer discussed in the previous section. The device draws an air sample containing particulates through an inlet port at a flow rate of a few liters per minute. The aethalometer collects the particle sample on a quartz fiber filter, and continually monitors the transmittance of the filter. Again, the time derivative of the signal is used to assess ambient aerosol absorption. There are a few small differences between the aethalometer and the PSAP however. In the aethalometer, the reference filter is placed adjacent to the active filter in the measurement chamber, but air is not pulled through the reference filter. Recall, in the PSAP the reference filter is placed after the active filter in the flow stream. The second difference is primarily the result of intended application of the technology. The aethalometer's intended purpose is often to measure the mass concentration of elemental carbon (soot) in the atmosphere. In fact, the device derives its name from the Greek word "*aethaloun*" – to blacken with soot. However, as we discussed in Section 3.4 there is a direct theoretical relationship between absorption coefficient and mass concentration of absorbing particles. If the mass absorption coefficient (m^2/g) of the aerosol is known the user can estimate the absorption coefficient from data. The trick is obtaining an accurate value for mass absorption coefficient for the specific aerosol sample and spectral range of the device being used. Magee scientific offers several aethalometer

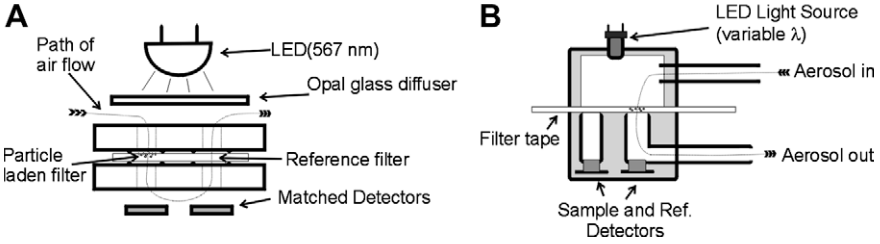

Fig. 10. Filter-based methods for measurements of aerosol absorption. (A) Illustration of a particle soot absorption photometer (PSAP). (B) Schematic of an aethalometer. Note the main difference is the flow path.

models that employ LEDs that span the entire near UV – near IR range (370, 470, 520, 590, 660, 880, and 990 nm). The device is usually equipped with a filter tape that is automatically moved when needed to prevent excessive particle loading on a particular filter (a third difference from the PSAP). Given the similarity to the PSAP, we might expect the aethalometer would also be subject to the same type of filter artifacts. This is in fact the case. Fortunately, these effects have been considered from both a theoretical perspective by Arnott et al. (2005) and empirically by Weingartner et al. (2003) and corrections for aethalometer filter loadings developed. It should be noted that despite the similarity between PSAP and aethalometer, the filter loading corrections are not identical due to differences between the filter media used for each method.

4.3.3. Multi-angle absorption photometer (MAAP)

In 2004, Petzold and Schonlinner (2004) reported a technique called multi-angle absorption photometry for measurement of aerosol absorption coefficient. In this technique, ambient air is sampled at ≈1 m^3/h and airborne particles are collected on a glass fiber filter tape. The filter is optically probed at 550 nm and filter transmittance is monitored. However, the reflectance of the filter is also measured by using additional detectors mounted at certain well-defined scattering angles. In monitoring these experimental parameters and use of a radiative transfer approximation aerosol absorption coefficient can be measured. The MAAP instrument offers an advantage over the PSAP and aethalometer in that correction of data for scattering is not required. However, in addition to the measurements the algorithm used to extract data requires input of asymmetry parameter (g) for the entire aerosol sample. The investigators used a value of 0.75 in their work but suggest a measurement error on the order of 5% is possible if a range of g values 0.5–0.86 is used instead. Petzold and Schonlinner also compared the performance of the MAAP with an aethalometer for measurements made at the Jungfraujoch in the Swiss Alps. Their analysis found measurements made with the MAAP are highly correlated with the aethalometer measurements, but the aethalometer b_{abs} measurements were on average a factor of 1.38 higher than the MAAP. Furthermore, these authors report a significant fraction of aethalometer measurements (even with 1 h averaging times) were negative, which is physically impossible. No such phenomenon was observed with the MAAP. The MAAP technology has been commercialized by Thermo Andersen (http://www.esm-online.de/andersen/product/CARUSSO-Brochure.pdf) who report a detection limit for elemental carbon of 20 ng/m^3 for a 30 min. measurement. If we assume a mass absorption coefficient of 10 m^2/g for black carbon a detection limit for b_{abs} on the order of 0.2 Mm^{-1} would be projected for the MAAP.

4.3.4. Photoacoustic spectroscopy

In 1999, Arnott et al. (1999) reported a photoacoustic spectrometer for measurement of light absorption (b_{abs}) by airborne particles. In this method, the aerosol is contained in an acoustic resonator and probed by a laser modulated at the resonant frequency of the device. Sample components which absorb light convert light energy into an acoustic wave that is detected by a microphone. The sample absorption coefficient (b_{abs}) is proportional to the acoustic pressure produced. A major advantage of the photoacoustic method compared to those mentioned in Sections 4.3.1,4.3.2,4.3.3 is the aerosol is probed while it is dispersed. This eliminates any uncertainties or correction schemes associated with collection on filters. An additional advantage is the magnitude of the measured signal scales with laser power so improvements in laser fluence can conceivably lower detection limits to the extent the aerosol sample is not altered or degraded by high irradiances. Additionally, the experimental apparatus is relatively simple and robust. The user must consider the potential for gas-phase absorbers (often O_3 or NO_2 in mid-visible) to interfere with analysis and scrub these gases from the sample or make background measurements. While the measurement wavelengths for the initial study were 532 and 685 nm, the method can easily be adapted for use at other wavelengths. For instance, a commercially available photoacoustic instrument (Droplet Measurement Technologies) makes measurements at 781 nm, however other wavelengths, and even a three wavelength model are available by special order. The 781 nm model was specifically designed to measure soot rather than absorption by wind-blown dusts. A more recent work by Lewis et al. (2008) describes a photoacoustic instrument capable of making measurements at 405 nm, which could be very useful for making absorption measurements of wind-blown dust. Impressive detection limits for b_{abs} of 0.08 Mm^{-1} for 60 s integration times have been reported (Lack et al., 2006).

4.3.5. Photothermal interferometry (PTI)

The technique of photothermal interferometry has been used to make laboratory measurements of light absorption by aerosols since the mid-1980's (Campillo et al., 1981; Fluckiger et al., 1985; Campillo and Lin, 1983). The PTI technique measures the effective phase shift in one arm of an interferometer induced by slight changes in the refractive index of the medium in that arm relative to a second arm. The refractive index change is caused by a slight temperature change resulting from light absorption. As such, the method is completely insensitive to elastic scattering of light. The method is capable of measuring extremely small changes in refractive index, and therefore very small optical absorptions. As you can imagine, vibrations and even instrument expansion due to temperature changes can potentially spell doom for interferometric techniques. To a large extent, this has limited more widespread use of the technique and delegated it to laboratory studies in which optical isolation can be employed and the system precisely controlled. Recently, Sedlacek has revived interest in the PTI technique through use of a more robust folded Jamin configuration for the interferometer (Sedlacek, 2006; Sedlacek and Lee, 2007). The optical requirements for this design are less stringent than in previous work, and allow a more compact design affording an instrument which is more suitable for field measurements of aerosol absorption coefficient. Sedlacek and Lee (2007) report the PTI instrument is capable of a precision of 0.2 Mm^{-1} and accuracy within 5%. A lower limit of detection for b_{abs} of 0.4 Mm^{-1} was also reported for a sample effective path length of only 5 cm. Interestingly, the authors also report slight differences in absorption coefficients measured by PTI as compared to use of the PSAP technique at high relative humidity.

4.4. Sun photometers

Sun photometers are devices which are pointed towards the sun to measure direct sun radiance over narrow wavelength bands. By comparing irradiances at earth's surface with expected values for the top of the atmosphere, the optical depth of the atmosphere can be computed. Gas absorption/scattering can be accounted for assuming a given atmosphere, and measured signals can be corrected for time of year, and angle of the sun in the sky (airmass). This can lead to direct measurement of column integrated aerosol optical depth for several wavelengths. Many sun photometers are mounted on robotic arms that can be programmed to precisely track the sun or make measurements at specific angles to the sun's location. Since aerosol optical depth can be measured at several wavelengths, the Angstrom extinction exponent (Section 3.5) can easily be extracted from the data. Since the efficiency with which light of different wavelengths is scattered varies considerably with particle size (see Fig. 4), the spectral optical depth data can be used to build a model of the aerosol particle size distribution which must be responsible for producing the unique Angstrom exponent signature (Schmid and Matzler, 1997). If both sun and sky radiances are collected additional aerosol properties can be retrieved. Almucantar scans of radiance as a function of scattering angle can yield data products such as aerosol complex refractive index, optical absorption, single scattering albedo, and the scattering phase function (Dubovik and King, 2000). Provisions for non-spherical particles such as dusts have also been built into the retrieval routines (Dubovik et al., 2006). All of these measurements are averaged over the total aerosol column within the atmosphere, so they truly provide complimentary data obtained by the point measurement techniques describe in Sections 4.1–4.3.

The Aerosol Robotic Network (AERONET) is an example of a global network of ground based CIMEL spectral radiometers than can measure both sun and sky radiances in several different spectral regions. The network has >500 sites globally, and simple data retrieval on the internet makes the AERONET program an extremely valuable resource for studies of the atmospheric aerosol. Indeed, the number of publications citing the AERONET program continue to grow at an ever increasing rate (>120 in 2007 compared to only 11 in 2000). A significant fraction of scholarly works we cite in Section 5 of this review involve AERONET data. Depending on the exact model of CIMEL radiometer used, AERONET data may be available for the following spectral channels: 0.34, 0.38, 0.44, 0.5, 0.675, 0.87, 1.02 and 1.64 μm. The Global Atmosphere Watch network of 12 Precision Filter Radiometers (GAW PFR) is another example of a sunphotometer network. These stations log aerosol optical depth and Angstrom exponent at wavelengths of 368, 415, 500 and 862 nm at 1–2 min frequency. Additional networks include Skynet, and the network maintained by the NOAA Earth Systems Research Laboratory (NOAA ESRL). Side-by-side comparisons of instruments used in each of these stations have even been provided by Kim et al., 2008). Another recent project of interest in the development and application of GLOBE sunphotometers. These very inexpensive, hand-held sunphotometers have been developed for use in education and feature LED's as detectors to measure aerosol optical thickness at 505 and 625 nm (Brooks and Mims, 2001).

5. Optical properties of wind generated dust

Entrainment of dust into the atmosphere is generally associated with strong, gusty winds in regions that are sparsely vegetated and are mostly arid (<250 mm precipitation annually). Emission of dust is inhibited by vegetation, surface obstructions such as snow, ice rocks etc... and elements such as high salt content and moisture which can have a binding effect on the soil. Recent satellite measurements as illustrated in Fig. 11 suggest dust aerosols are largely a Northern Hemisphere phenomenon, with a large fraction of emissions centered in a "*dust belt*" which extends from North Africa through the Arabian Peninsula to Central Asia and China (Liu et al., 2008; Hu and Sokhi, 2009). Most dust generated in the southern hemisphere appears to originate in Australia. Certain dust source "hot-spots" can often be identified from satellite imagery (Lee et al., 2009) and sometimes these locations coincide with topographic depressions. Some examples of these are the Bodélé Depression in Chad, the Tarim Basin (Taklimakan Desert) in China, and Lake Eyre in Australia. The Sahara is believed to be a major player in the global dust budget, and desert regions in the Middle East are also significant players as are deserts in Mongolia and Northern China (Taklimakan and Badain Jaran deserts) (Zhang et al., 2003). We have chosen to organize this section of the review by discussing the optical properties of dusts recently reported in the literature at varying locations within the Northern Hemisphere dust belt and Australia. Whenever possible, our focus is on the optical properties of dust near source regions and during significant dust events rather than long-range transport/atmospheric processing.

5.1. Western Africa

Approximately 130–760 Tg of dust is believed to originate from the Sahara desert annually (Laurent et al., 2008; Engelstaedter et al., 2006; Goudie and Middleton, 2001). As such, characterizing the optical properties of this dust is important to accurately describe radiative transport in the atmosphere. It is not surprising that characterization of this dust has been the focus of several major research efforts in recent years. The Saharan mineral dust experiment (SAMUM) is a recent effort to better understand both the shortwave and longwave properties of mineral dust aerosol in the western Saharan region. Results from this study obtained in 2006 for various sites in Morocco have recently been disseminated in a special issue of Tellus (vol. 61(1), 1–353, 2009). Additional recent campaigns include the Dust and Biomass Experiment (DABEX 2006), the Dust Outflow and Deposition to

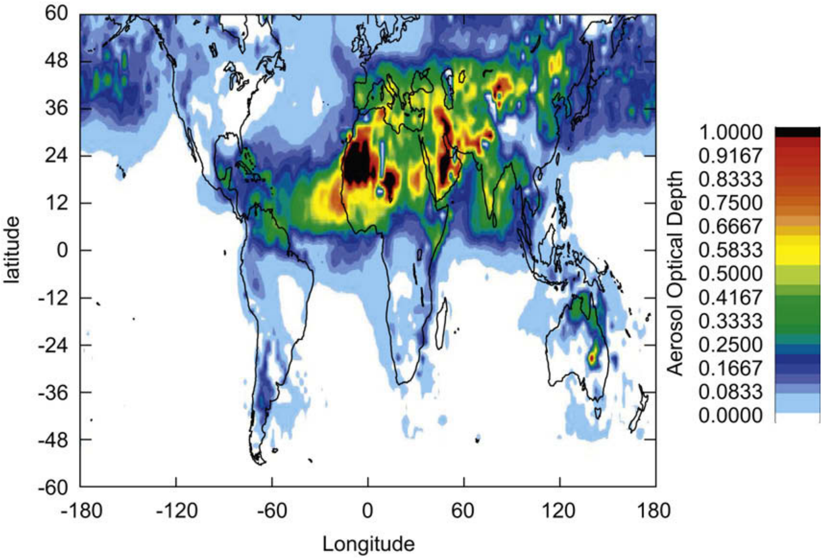

Fig. 11. Map of dust optical depth at 360 nm during spring 2003 as retrieved from satellite measurements. The Sahara, Gobi, and Australian deserts can clearly be seen as strong dust emission sources. In addition, transport of dust over the Atlantic can be observed. Reproduced with permission from Hu and Sokhi (2009).

the Ocean Experiment (DODO 2006), and the Saharan Dust Experiment (SHADE 2000).

As part of SAMUM, Shladitz et al. have reported on the optical and physical properties of Saharan dust at a surface site at Tinfou, Morocco (Schladitz et al., 2009). These authors have used SEM with energy dispersive X-ray analysis to study the size-resolved composition of Saharan dust. The authors found a bimodal particle size distribution dominated by ammonium sulfate particles below 500 nm diameter and mineral dusts above 500 nm. Particles between 0.5 and 10 μm contained silicates, quartz, calcium carbonates, and light absorbing oxides of iron. The authors report a value of 1.53 for the real component of the refractive index at wavelengths of 537 nm and 637 nm and imaginary parts of 0.0041 and 0.0031 at those wavelengths. Albedo at 537 nm was 0.96 while at 637 nm it was 0.98. Backscatter fraction, as measured by a TSI nephelometer, was reported to be 0.09–0.10. Angstrom absorption exponents were generally in the range of 3.75–5 for the dust while Angstrom scatter exponents were near 0 and at times slightly negative (0–0.15). This is in agreement with the results of Müller et al. (2009b) who have reported values of 4.35 and 6.41 for Angstrom absorption exponents for re-suspended dust collected in Morocco and Burkina Faso. A companion publication reports imaginary parts of refractive index for Saharan dust (after a correction for soot absorption) to be 0.0051, 0.0016, and 0.00045 at wavelengths of 450, 550, and 650 nm for a site in southern Morocco (Müller et al., 2009a). A third study from SAMUM focused on airborne measurements and reports a real index of $n = 1.55–1.56$ for the Saharan dust which was observed to be nearly constant across the 450–700 nm window (Petzold et al., 2009). Alternatively, the imaginary part if the index varied considerably across this spectral window. The authors report values of $k = 0.0031–0.0052$ at 450 nm, 0.0003–0.0025 at 700 nm. Interestingly, values of the imaginary part of the refractive index seem to be correlated to different particulate source regions. Dust believed to originate in the Atlas forelands near Morocco/Algeria had an imaginary part of 0.0049 and 0.0017 at 450 and 700 nm and demonstrated an absorption Angstrom exponent of 3.6–3.8. Dust originating further east from the lowlands and salt-lakes of north eastern Algeria and Tunisia exhibited $k \approx 0.003$ and 0.0003 at 450 and 700 nm and correspondingly a much larger absorption Angstrom exponent of 6–6.6. These results highlight the importance of source region for characterization of the optical properties of wind-blown dust.

As part of the Dust Outflow and Deposition to the Ocean project (DODO) McConnell et al. has reported refractive indices (550 nm), asymmetry parameter (550 nm), and Angstrom exponents (550–700 nm) during the dry and wet season based on aircraft measurements taken near Dakar, Senegal (McConnell et al., 2008). The real portion of the refractive index was 1.53 for both February (dry season) and August (wet season). However, the imaginary part changed from 0.0005 to 0.0014 indicating that the dust seemed to be more absorbing in the wet season. An asymmetry parameter of 0.68 at 550 nm was suggested and the average Angstrom exponent for the Saharan dust influenced air mass was near 0. Osborne et al. (2008) have reported a refractive index of $1.53 + 0.0004i$ and asymmetry parameter of 0.71 for campaign averaged values from DABEX 2006. Similarly, the report of Haywood et al. (2003) from SHADE 2000 suggests a value of $1.53 + 0.0015i$ and 0.72 for refractive index and asymmetry parameter. A study by Derimian et al. (2008a) in M'Bour, Senegal provided Angstrom Exponents for both mixed aerosols and dust aerosols. The mixed aerosol was present January 21, February 3 and 4 with values of 0.85, 0.89, 0.92, respectively. The coarse mode dust dominated aerosol was present March 10 and 31 with values of 0.11 and 0.19, respectively. Derimian et al. (2008a) also provide albedo data for these two dust events. The first event, gave SSA values of 0.91 at 440 nm and 0.98 at 1020 nm. The second event, gave SSA values of 0.88 at 440 nm and 0.93 at 1020 nm. Comprehensive chemical composition data was not presented in this study so it is not clear whether the differences in optical data between March 10 and 31 were caused by differences in dust composition or local contamination/alteration of the particles.

Certain optical properties of Saharan dust on the west coast of Africa reported by many authors over several field campaigns seem to be in relatively good agreement. For the real portion of refractive index, values over the narrow range of 1.53–1.56 have been reported. The imaginary part of refractive index is more variable, and values between 0.0003 and 0.005 have been reported for the visible spectral region. As previously mentioned, some evidence has been presented linking imaginary index to source regions and wet/dry season. Angstrom exponent for Saharan dust aerosols is generally <0.5, and often near zero. However, Angstrom absorption exponents for Saharan dusts can vary between 3 and 7, likely owing to the variable composition of light absorbing hematite and goethite. Asymmetry parameters in the range of 0.68–0.72 seem to be commonly encountered.

5.2. Eastern Sahara, Arabian Peninsula, and Middle East

El-Metwally et al. (2008) has studied the optical properties of aerosols in Cairo with sun photometry as part of the NASA AERONET program. Clearly, Cairo is an urban center which can complicate the de-convolution of the effects of dust aerosols from other aerosol classes. The authors classify an aerosol as being "dust-like" through air mass back trajectory calculations and by an Angstrom exponent <0.5. However, the potential for contamination by the urban plume remains. Using these criteria, the authors report a real portion of the refractive index of 1.46–1.54 over the spectral region of 441–1022 nm and an all wavelength average of 1.51. The imaginary portion of the refractive index was given constant as 0.002 for the same spectral region while the single scatter albedo ranged from 0.934 to 0.965 for the "dust-like" aerosol. Asymmetry parameter (g) ranged from 0.661 to 0.681 for these wavelengths.

Linke et al. (2006) conducted a laboratory study of Saharan dust samples that were collected from different regions and re-suspended. Two samples collected in/near Cairo had Angstrom Exponents of 0.56 and 0.45. Linke et al. also provide SSA data for the Cairo sample and a Moroccan sample. The Cairo sample had a SSA of 0.99 for both 532 nm and 1064 nm, but only 0.76 for 266 nm. The Moroccan sample had SSA of 0.63 for 266 nm but 0.98 for 532 nm. Both dust samples clearly have strong absorption at 266 nm, but the atmospheric importance of this is unclear given the actinic cut at 290 nm. This study also generated an aerosol sample by artificial means which could possibly alter particle size distributions and optical properties from that observed in the atmosphere.

The Bodélé Depression in Chad has been described as the dustiest place on earth. It has been estimated that dust emission from this region can exceed 1 Tg per day during significant dust events! Interestingly, dust in this region is dominated by fossil diatoms from the dry lake bed which comprises the depression. The optical properties of dust from this region was a focus of study during the BoDex 2005 campaign. Optical data for particles in this region were reported for the BoDEx 2005 campaign by Todd et al. (2007). At 440 nm the refractive index was $1.46 + 0.002i$, at 670 nm it was $1.47 + 0.001i$, at 870 nm it was $1.45 + 0.001i$ and at 1020 nm it was $1.44 + 0.001i$. The mean Angstrom extinction exponent was 0.24 with a range of 0.06–0.45. Reported single scatter albedo values were 0.969, 0.986, 0.989, and 0.990 for 440, 670, 870, and 1020 nm, respectively. These albedo values are higher than values reported for other Saharan dusts, which speaks to the unique composition of particulates from Bodélé.

Dubovik et al. (2002b) presents data for an 8 year study of worldwide locations by the AERONET network of ground-based radiometers. Desert dust was studied in Bahrain (Persian Gulf), and Solar Village, Saudi Arabia. In Bahrain, the real component of the refractive index was 1.55 while the imaginary component varied considerably with wavelength. The values for the imaginary component are 0.0025, 0.0014, 0.001, and 0.001 at 440 nm, 670 nm, 870 nm and 1020 nm, respectively. Single scatter albedo ranged from 0.92 to 0.97, increasing with wavelength, and asymmetry parameter ranged from 0.66 to 0.68 for these wavelengths. Angstrom exponent varied widely from 0 to 1.6. This reflects the varying sources/composition of particulate matter at this location (Bahrain has a significant amount of fine particles produced by industry). In Solar Village Saudi Arabia, the real component of the refractive index was reported to be 1.56. The values for the imaginary component are 0.0029, 0.0013, 0.001, and 0.001 at 440 nm, 670 nm, 870 nm and 1020 nm, respectively. Single scatter albedo is reported to be 0.92–0.97 with a range of *g* values between 0.65 and 0.69. The Angstrom exponent varied from 0.1 to 0.9. Dermimian et al. (2008b) also provide SSA data for Solar Village, Saudi Arabia. In this report, SSA was 0.90 at 440 nm and 0.97 at 1020 nm. These authors also provide data for other locations in the region. In Sede Boker, Isreal the SSA was 0.91 at 440 nm and 0.96 at 1020 nm. In Bahrain, the SSA was 0.90 at 440 nm and 0.97 at 1020 nm.

Eck et al. (2008) have studied the optical properties of the aerosol over several sites in the United Arab Emirates in summer. These authors found typical albedo values during a dust event were 0.91–0.93 for 440 nm and 0.95–0.98 for 1020 nm. The particle size distribution data extracted from experimental data indicated a volume average radius around 2.2 μm and Angstrom extinction exponents on the order of 0.2–0.3 were reported for this event.

5.3. Northern India

Pandithurai et al. (2008) have reported on the optical properties of dust aerosols in New Delhi believed to originate from the Thar desert and other neighboring regions. This region is frequently influenced by wind-blown dust originating in the Thar desert during the pre-monsoon period (April–June). However, the aerosol at this location would be expected to be significantly impacted by anthropogenic activities since Delhi is a major urban area. The authors used a sun/sky radiometer manufactured by PREDE, Ltd. to obtain their data and an improved Langley method for calibration. The study spanned from March to June 2006 and the authors noted an increase in dust aerosol loading over the course of the study. The authors reported a 2–3 fold increase in coarse mode particles from April to June when dust events occur. These authors reported an average single scattering albedo (SSA) value of 0.79 during the pre-monsoon season for 500 nm wavelength. SSA monthly averages for March, April, May and June 2006 were 0.84, 0.78, 0.75 and 0.74, respectively. The authors found that the SSA increases with wavelength due to the coarse mode particles. Refractive indices were also extracted from the data for 500 nm. For the months of May and June when the aerosol was most dominated by dust, the monthly averages for the real component were 1.54 for both months. For the imaginary component, 0.022 for May was reported and 0.024 for June. The mean Angstrom exponent itself was found to decrease from 1.28 in March to 0.47 in June. This effect was attributed to the increase of coarse particles due to dust storms. Reported asymmetry parameters for visible wavelengths ranged from 0.70 to 0.76 for the month's of May and June.

Another study in India was conducted over Delhi in 2003 by Singh et al., 2005). Measurements were obtained for the pre-monsoon period (April–June). The authors reported an approximate average of the extinction Angstrom exponent to be 0.328 during the entire pre-monsoon season (range of values $\alpha = -0.2\text{–}1$). On days with strong sand storms, negative values were obtained for the Angstrom Exponent; the authors provide the value of -0.06 for June 6, 11 and 18. This low Angstrom Exponent value indicates a dominance of coarse particles present. The authors used the Optical Properties of Aerosols and Clouds (OPAC) model to estimate values for the single scattering albedo and the asymmetry parameter at $\lambda = 500$ nm and 50% relative humidity. The single scatter albedo reported was 0.672 and the asymmetry parameter was 0.790. The low values of the SSA was attributed to the mixture of urban and desert aerosol present in Delhi, however the SSA was found to increase with wavelength which is a trend often seen for a dominance of coarse mode particles.

Dey et al. (2004) have reported data obtained from AERONET measurements in Kanpur taken by a CIMEL sky radiometer. In this area of India there is a bimodal size distribution. The fine mode is the range of 0.08–0.2 μm and the coarse mode is around 5 μm. During the pre-monsoon and monsoon season there is a higher volume concentration of coarse mode particles. The authors reported that after a dust event the volume concentration of the coarse mode is three times higher and there is no change in the volume concentration of the fine mode particles. The authors reported Angstrom Exponent values for May 2001 and May 2002 to be 0.4 and 0.33, respectively. They also reported that following dust events the Angstrom Exponent can decrease by 70–90% to below 0.25 and even be a negative value. This reflects the dynamic nature of the aerosol in this urban region. An example of this is provided with a measurement of 0.24 was taken May 14 2001 following a mild dust storm. Dey et al. report (as estimated from Fig. 2 of their work) single scatter albedo values of ≈0.89–0.96 for 440–1020 nm wavelength range during the period when the Angstrom exponent was low (<0.25) indicating significant dust presence. These authors also report the refractive index values for Kanpur with the dust originating from the Thar desert. The average value for May 2001 was $1.495 + 0.004i$ and for May 2002 was $1.541 + 0.002i$, both for 670 nm. Again, it is unclear the degree to which the dust has been modified through atmospheric processing or is externally mixed. It was noted that after dust events the real component increased while the imaginary component tended to decrease, this was true on all but one occasion. The wavelength dependence of the real and imaginary component of refractive index can be ascertained from Fig. 2 of their work. For the real component, Fig. 2 of their work suggests values ranging between 1.32 and 1.6 are encountered for 440 nm. Values between 1.45 and 1.6 appear to be typical when significant dust is present for 670–1020 nm. An imaginary component of 0.003 was often encountered for the 440 nm channel, while values in the 0.0015–0.002 range appear typical of 670–1020 nm region.

Another study reporting AERONET data was written by Singh et al. (2004). This study reported values for different seasons in Kanpur, rather than just focusing on data obtained in May. The authors reported that in the winter season the SSA was lower than other seasons, always below 0.85, and it is very wavelength dependent. This could be the result of the influx of black carbon during the heating season. During pre-monsoon and monsoon season the SSA is higher, always above 0.9. Dust aerosols during these seasons contribute to a higher SSA value at higher wavelengths while the opposite trend occurs in dust free conditions. These authors also reported Angstrom exponents for the different seasons of Kanpur. The average Angstrom Exponent in the winter months was 1.26. It decreased to an average of 0.6 in the pre monsoon season, and then 0.66 during Monsoon season. The Angstrom exponent value during post monsoon was 1.12. Again, this is consistent with coarse dust having a significant impact during the pre-monsoon season.

There appears to be some discrepancy on the optical properties of dusts originating from the Thar desert in northwestern India. In some studies, albedo (SSA) values <0.75 are reported, while in others it is suggested a value of >0.9 is typical. The low values for SSA are considerably lower than reports of wind-blown dusts for alternate regions such as Saharan Africa. This is conceivable since dust composition varies locally. Further evidence supporting the idea Thar desert dust is more strongly absorbing is the work of Moorthy et al. (2007) who have reported albedo values between 0.88 and 0.94 for Thar desert dust. These authors inferred Thar desert dust is simply just more absorbing when compared to Saharan dust. Another possibility (particular for measurements in Delhi) is that the very low albedo values reported (and correspondingly high *k* values) are the result of anthropogenic influences. Delhi is a metropolis of nearly 16 million inhabitants. It has been suggested the accumulation of other species (such as soot) on dust while airborne can significantly affect its optical properties. Clarke et al. (2004) indicated that pollution enables the uptake of volatile compounds onto the surface of coarse dust. This effect alters the optical properties of the dust, for example the SSA is lowered. Additional research is necessary to parameterize this type of effect.

5.4. East Asia/China

Eastern Asia has been estimated to be the source of some 240,000–650,000 Gr/yr of wind-blown dust (Huebert et al., 2003). From 2001 to 2005, the Aeolian Dust Experiment on Climate impact (ADEC) conducted field observations of particulate matter over China and Japan (Mikami et al., 2006). As the goal of this project was to better understand the impact of aeolian dust on climate, the optical properties of wind blown dust were of keen interest. As part of this study Uchiyama et al. (2005a) have retrieved single scatter albedo values from sky radiometer data, and measured albedo directly in the mid-visible (530 nm) with a PSAP and a nephelometer for a location in Qira, China in the southern portion of the Taklimakan desert. These authors report an albedo of 0.933 from the retrieval and 0.91–0.93 as measured. In a companion work, the authors observe Angstrom exponents for Qira and Aksu, China in the northern Taklimakan to be consistently below 0.4, indicative of coarse mode particles (Uchiyama et al., 2005b). For calculations, these authors used a value of $1.50 + 0.005i$ for refractive index. Shi et al. (2005) have also reported values of refractive index for east Asian dust. The real component reported by these authors was approx. 1.5 while the imaginary component decreases from 0.007 to 0.0023 over the spectral window 400 to 700 nm. These authors report a value of 0.00411 for 500 nm wavelength which compares well with a value reported for Central Asian dust (0.004) by Sokolik and Golitsyn (1993). The authors also used Mie theory to estimate single scatter albedo and asymmetry parameter (*g*). The authors report a variable albedo from 0.60 to 0.81 over 400 to 700 nm which increases with wavelength. The asymmetry parameter was reported to be 0.87–0.92 for their modeled dust over the same spectral range. It should again be noted these are calculated values. Cheng et al. (2006) have also studied the optical properties of dust aerosols in China. These authors report the real component to refractive indices for sites near dust source regions (Dunhuang, Yulin, Inner-Mongolia) as 1.41–1.45 at 440 nm, 1.49–1.53 at 670 nm, and 1.53–1.54 at 870 and 1020 nm. The averages of imaginary index were 0.0017–0.0018 at 440 nm, 0.0015–0.0016 at 670 nm, 0.0017–0.0018 at 870, and 1020 nm for the same sites. As would be expected, Angstrom exponent for these sites were low, particularly in the spring (April) when the monthly average Angstrom exponent was 0.12 for Dunhuang and 0.19 for Yulin. Derimian et al. (2008b) provide single scatter albedo estimates for Dunhuang, China an oasis town in the Kumtag desert. The reported SSA was 0.93 at 440 nm and 0.98 at 1020 nm. Finally, the aircraft measurements of Clarke et al. (2004) made in the Asian outflow suggest an imaginary component of the Asian dust refractive index equal to 0.0006 (1.53 as real portion). The authors suggest this implies a single scatter albedo of 0.9 – 0.99 depending on particle size, but mention a field campaign average value of 0.97.

5.5. Australia

Qin and Mitchell (2009) have recently considered aerosols over Australia. These authors conducted cluster analysis of inversions of sky radiance distributions from ground stations and found four classes or "clusters" of aerosol types. Class 2 was identified as coarse dust with an effective radius of 2.2 μm. The Angstrom exponent extracted from their analysis was 0.04 over the spectral range 440–1020 nm for this class of aerosol. The single scatter albedo was 0.94 at 440 nm and increased with wavelength (0.977 at 870 nm). An asymmetry parameter of 0.74 was reported at 440 nm, but *g* decreased to approximately 0.72 for the spectral range between 600 and 1020 nm. The authors reconstructed refractive index based on the chemical composition and a mixing rule and have reported a value of 1.545 for the real component and 0.0018 as the imaginary component. Qin and Mitchell also point out that since the hematite content is higher in the southern portion of the continent the refractive index would be expected to vary with location. The authors also report the hematite content of Australian soils may be slightly higher than dusts originating in the northern hemisphere "dust belt" leading to stronger light absorption.

5.6. Summary of observed optical properties

Fig. 12a illustrates a plot of the real and imaginary portion of refractive indices as a function of wavelength of dust considered in this review. The real component seems to be relatively constant ≈1.5, but does vary between 1.43 and 1.56 depending on source. The imaginary portion of refractive index reported seems to be significantly more variable. This is likely a consequence of differences in dust composition at each location. While we have focused mainly on observationally based data, inferring dust optical properties based on chemical composition is also actively pursued (Lafon et al., 2006; Kandler et al., 2007). This approach is promising given the large quantity of data available on chemical composition of earth's soils. What is consistent within the dataset we have examined is *k* increases with decreasing wavelength. This parallels the trend in *k* value for hematite which increases from ≈0.05 to 1 with decreasing wavelength over the visible spectral range (Sokolik and Toon, 1999). The studies considered in this work suggest $k \approx 0.003$–0.004 is typical for mid-visible wavelengths (500 nm). Fig. 12b illustrates a plot of single scatter albedo as a function of wavelength for dusts considered. For the visible region, albedo values of ≈0.91 for 440 nm seem to be a rough average. Albedo tended to increase to ≈0.98 near 670 nm and into the near IR. Again, this is consistent with increase absorption at shorter wavelengths.

6. Conclusion

In recent years, significant progress has been made in describing the optical properties of wind-blown dusts yet many challenges remain. In the area of modeling, the consideration of nonspherical particles will remain a focus of research into the foreseeable future. DDA and FDTD codes for irregular particles with or without inclusions can be improved and computation speed increased such that larger particles can be considered. Furthermore, improvements in computational speed would allow systematic

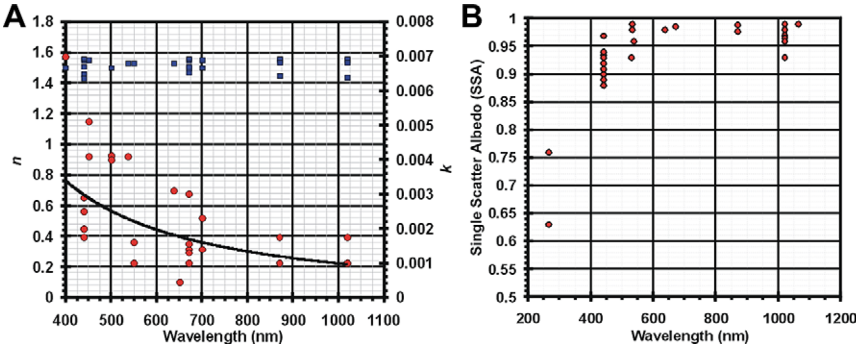

Fig. 12. (A) Plot of observed real (blue squares) and imaginary (red circles) components to refractive index values vs. wavelength for dust considered in this review. One study was omitted as it appeared to be an outlier. Imaginary index (k) is plotted on second y-axis for clarity. The real portion of refractive index was near 1.5 for all studies and the imaginary component exhibits strong wavelength dependence with enhanced absorption in the blue. This is consistent with the absorption spectrum of hematite. (B) Plot of reported single scatter albedo vs. wavelength for dust considered in this review. In most cases albedo was >0.9 for the visible region and typically decreased with decreasing wavelength. (For interpretation of the references to color in this figure legend, the reader is referred to the web version of this article.)

study of the effect of coating thickness and shape effects on the optical properties of irregular dusts. This type of modeling study could prove very useful to develop generalizations regarding the optical properties of internally mixed dusts. In parallel with the advancement of the computational codes, an improved understanding of the physical transformation of dust in the atmosphere should be developed (discussed below). This will allow construction of an empirically based model for typical aged dust particles to consider for computational modeling

The last decade has seen tremendous advances made in measurement technologies available for the optical characterization of aerosols. This is particularly true of the recently introduced techniques for measurement of aerosol absorption such as photoacoustic spectroscopy or photothermal interferometry. The main advantage of these techniques is highly sensitive measurements can be made on dispersed aerosols. This eliminates the need for cumbersome and unsatisfying data correction schemes. The introduction of cavity ring-down spectroscopy for aerosol extinction measurement in both pulsed and cw format has allowed bench-top scale aerosol extinction measurements to be made. Future work in these areas should focus on making these advanced measurement techniques more affordable and more available to the research community. Better instrument access will allow higher quality data sets to be recorded which will undoubtedly improve our understanding of the optical properties of dust. A specific instrument of interest yet to be developed (to best of our knowledge) is a polar nephelometer capable of rapid, angular resolved measurements of ambient aerosols. Such an instrument in theory would provide phase function, backscatter fraction, and total aerosol scatter coefficient. The instrument could be of use to study scattering of non-spherical particles from an experimental point of view. This would help validate and support computational approaches.

Our knowledge of the optical properties of dusts has seen substantial improvement during the last decade. An example of this progress is reflected in estimates of light absorption by mineral dusts. It was previously thought that a good estimate of the imaginary portion of refractive index for dust in the mid-visible was $k = 0.008$ (WMO, 1983). However, the seminal works of Kaufman et al. (2001), Dubovik et al. (2002b), Tanré et al. (2003) and subsequent measurements by authors cited in Section 5 indicate dust is less absorbing than previously believed. A more recent estimate of the mid-visible value of $k \approx 0.003$–0.004 appears to be more accurate. Additionally, the development and subsequent use of the spheroid model to account for dust non-sphericity has been a major development. As mentioned in Section 3.6, the spheroid model allows much more accurate modeling of phase function and polarization of scattered light from dusts than that achievable through a model based on Mie spheres.

A significant future direction may be continued investigations of the chemical and physical processing of atmospheric dusts during long-range transport. While the intent of this review inasmuch as possible has been to focus on optical properties of wind-blown dusts in its native state, it is important to consider dispersed dust does not exist in a vacuum. Dust particles can be chemically and physically modified in the atmosphere which can alter observed optical properties. It is well-known mineral dusts can serve as surfaces for heterogeneous chemical reactions in the atmosphere (Usher et al., 2003). Some of these reactions may result in a mineral dust particle becoming associated with, coated, or embedded within a matrix not characteristic of mineral dust composition. This would be expected to alter the optical properties of a given particle significantly. For instance, particle shape and surface roughness could be influenced. Additionally, particle projected diameters would likely be altered which would manifest itself as a change in scattering cross section. Additionally, it is known that coatings on soot particles can enhance particle absorption (Bond et al., 2006). A similar effect for mineral dusts could easily be envisioned.

Field evidence for this type of atmospheric chemical processing can be found in the works of Hwang and Ro (2005, 2006). These authors used electron probe X-ray microanalysis to characterize Asian dust collected at ChunCheon, Korea. The authors report all four samples considered experienced chemical modification (sulfate, nitrate formation) during long-range transport. The chemical processing of Asian mineral dust has also been observed by Sullivan et al. (2007) through single particle mass spectrometry. These authors have found that secondary acids, chloride, and ammonium can accumulate on mineral dusts in the atmosphere. Interestingly, nitrate seemed to accumulate on dust rich in calcium, and large amounts of sulfate accumulated on aluminosilicate rich dusts. Sullivan et al. suggest the enhanced sulfate level in the aluminosilicate rich dusts could be a consequence of its iron content. Aqueous ferric ions are known to catalyze the oxidation of SO_2 to sulfate aerosol (Finlayson-Pitts and Pitts, 2000) which could explain the enhancement. Aqueous ions of iron are also known to catalyze the decomposition of hydrogen peroxide (Fenton reaction) which could affect hydroxyl radical concentrations. This presents an additional possible mechanism by which mineral dust particles can enhance formation of coatings on their surfaces.

Despite the evidence for chemical transformations on mineral dust surfaces, we are not aware of any comprehensive study of the alteration of dust optical effects via atmospheric processing and the time course associated with this process. These types of studies are needed to further advance our understanding of the scattering and absorption of light by mineral dusts in the atmosphere – particularly as a function of time after dispersal. While most data we present in Section 5 describes field measurements, future chemical processing studies can be carried out in a controlled laboratory setting and the advanced measurement techniques described in Section 4 can be applied to the problem. A lab setting would also allow precise control over variables likely to influence the rate and extent of chemical processing such as relative humidity and concentration of reactants. While dust does not typically get dispersed into the atmosphere at high local relative humidity, dust can be transported large distances from source regions. As such, the effect of relative humidity itself on the optical properties of dispersed mineral dusts should also be studied.

References

Abo Riziq, A., Trainic, M., Erlick, C., Rudich, Y., 2008. Extinction efficiencies of coated absorbing aerosols measured by cavity ring down aerosol spectrometry. Atmos. Chem. Phys. 8, 1823–1833.

Anderson, T.L., Ogren, J.A., 1998. Determining aerosol radiative properties using the TSI 3563 integrating nephelometer. Aerosol Sci. Technol. 29 (1), 57–69.

Arnott, W.P., Moosmuller, H., Sheridan, P.J., Ogren, J.A., Raspet, R., Slaton, W.V., Hand, J.L., Kreidenweis, S.M., Collett, J.L., 2003. Photoacoustic and filter based ambient aerosol light absorption measurements: instrument comparisons and the role of relative humidity. J. Geophys. Res. 108 (D1), 4034. doi:10.1029/2002JD002165.

Arnott, W.P., Hamasha, K., Moosmuller, H., Sheridan, P.J., Ogren, J., 2005. Towards aerosol light absorption measurements with a 7-wavelength aethalometer: evaluation with a photoacoustic instrument and 3-wavelength nephelometer. Aerosol Sci. Technol. 39, 17–29.

Arnott, W.P., Moosmuller, H., Rogers, C.F., Jin, T., Bruch, R., 1999. Photoacoustic spectrometer for measuring light absorption by aerosol: instrument description. Atmos. Environ. 33, 2845–2852.

Babenko, V.A., Astafyeva, L.G., Kuzmin, V.N., 2003. Electromagnetic Scattering in Disperse Media: Inhomogeneous and Anisotropic Particles. Praxis, Chichester, UK.

Barkey, B., Liou, K.N., 2001. Polar nephelometer for light-scattering measurements of ice crystals. Opt. Lett. 26 (4), 232–234.

Barkey, B., Paulson, S.E., Chung, A., 2007. Genetic algorithm inversion of dual polarization polar nephelometer data to determine aerosol refractive index. Aerosol Sci. Technol. 41, 751–760.

Beuttell, R.G., Brewer, A.W., 1949. Instruments for the measurement of the visual range. J. Sci. Instrum. 26, 357–359.

Bohren, C.F., Huffman, D.R., 1983. Absorption and Scattering of Light by Small Particles. Wiley, New York.

Bond, T.C., Anderson, T.L., Campbell, D., 1999. Calibration and intercomparison of filter-based measurements of visible light absorption by aerosols. Aerosol Sci. Technol. 30, 582–600.

Bond, T.C., Habib, G., Bergstrom, R.W., 2006. Limitations in the enhancement of visible light absorption due to mixing state. J. Geophys. Res. 111, D20211. doi:10.1029/2006JD007315.

Borghese, F., Denti, P., Saija, R., 2007. Scattering From Model Nonspherical Particles. Theory and Applications to Environmental Physics. Springer, Berlin.

Brooks, D.R., Mims III, F.M., 2001. Development of an inexpensive handheld LED-based Sun photometer for the GLOBE program. J. Geophys. Res. 106, 4733–4740.

Bulatov, V., Fisher, M., Schechter, I., 2002. Aerosol analysis by cavity-ring-down laser spectroscopy. Anal. Chim. Acta 466, 1–9.

Butler, T.J.A., Miller, J.L., Orr-Ewing, A.J., 2007. CRDS measurements of single aerosol particle extinction part 1. The effect of position of a single particle within the laser beam on extinction. J. Chem. Phys. 126, 174302.

Campillo, A.J., Dodge, C.F., Lin, H.B., 1981. Aerosol particle absorption spectroscopy by photothermal modulation of Mie scattered light. Appl. Opt. 20, 3100–3102.

Campillo, A.J., Lin, H.-B. 1983. Method and Apparatus for Aerosol Particle Absorption Spectroscopy, US Patent 4,415,265.

Cheng, T., Wang, H., Xu, Y., Li, H., Tian, L., 2006. Climatology of aerosol optical properties in Northern China. Atmos. Env. 40 (8), 1495–1509.

Clarke, A.D., Shinozuka, Y., Kapustin, V.N., Howell, S., Huebert, B., Doherty, S., Anderson, T., Covert, D., Anderson, J., Hua, X., Moore, K.G., McNaughton, C., Carmichael, G., Weber, R., 2004. Size distributions and mixtures of dust and black carbon aerosol in Asian outflow: physiochemistry and optical properties. J. Geophys. Res. 109, D15S09. doi:10.1029/2003JD004378.

Cook, B.I., Miller, R.L., Seager, R., 2009. Amplification of the North American dust bowl drought through human-induced land degradation. Proc. Nat. Acad. Sci. 106 (13), 4997–5001.

Cwiertny, D.M., Young, M.A., Grassian, V.H., 2008. Chemistry and photochemistry of mineral dust aerosol. Annu. Rev. Phys. Chem. 59, 27–51.

Dave, J.V., 1968. Subroutines for computing the parameters of the electromagnetic radiation scattered by a sphere. Rept. No. 320-3237, IBM Scientific Center, Palo Alto, CA.

Derimian, Y., Leon, J.-F., Dubovik, O., Chiapello, I., Tanre, D., Sinyuk, A., Auriol, F., Podvin, T., Brogniez, G., Holben, B.N., 2008a. Radiative properties of aerosol mixture observed during the dry season 2006 over M'Bour, Senegal (African Monsoon Multidisciplinary Analysis campaign). J. Geophys. Res. 113, D00C09. doi:10.1029/2008JD009904.

Derimian, Y., Karnieli, A., Kaufman, Y.J., Andreae, M.O., Andreae, T.W., Dubovik, O., Maenhaut, W., Koren, I., 2008b. The role of iron and black carbon in aerosol light absorption. Atmos. Chem. Phys. 8, 3623–3637.

Dey, S., Nand, S., Tripathi, N., Singh, R.P., Holben, B., 2004. Influence of dust storms on the aerosol optical properties over the Indo-Gangetic basin. J. Geophys. Res. 109, D20211. doi:10.1029/2004JD004924.

Doicu, A., Eremin, Y.A., Wriedt, T., 2000. Acoustic and Electromagnetic Scattering Analysis using Discrete Sources. Academic Press, San Diego.

Doicu, A., Wriedt, T., Eremin, Y.A., 2006. Light Scattering by Systems of Particles. Null-field Method with Discrete Sources: Theory and Programs. Springer, Berlin.

Dubovik, O., King, M.D., 2000. A flexible inversion algorithm for retrieval of aerosol optical properties from Sun and sky radiance measurements. J. Geophys. Res. 105, 20673–20696.

Dubovik, O., Sinyuk, A., Lapyonok, T., Holben, B.N., Mishchenko, M., Yang, P., Eck, T.F., Volten, H., Munoz, O., Veihelmann, B., van der Zande, W.J., Leon, J.-F., Sorokin, M., Slutsker, I., 2006. Application of spheroid models to account for aerosol particle nonsphericity in remote sensing of desert dust. J. Geophys. Res. 111. doi:10.1029/2005JD006619.

Dubovik, O., Holben, B.N., Lapyonok, T., Sinyuk, A., Mishchenko, M., Yang, P., Slutsker, I., 2002a. Non-spherical aerosol retrieval method employing light scattering by spheroids. Geophys. Res. Lett. 29 (10). doi:10.1029/2001GL014506.

Dubovik, O., Holben, B., Eck, T., Smirnov, A., Kaufman, Y.J., King, M.D., Tanre, D., Slutsker, I., 2002b. Variability of absorption and optical properties of key aerosol types observed in worldwide locations. J. Atmos. Sci. 59, 590–608.

Eck, T.F., Holben, B.N., Reid, J.S., Sinyuk, A., Dubovik, O., Smirnov, A., Giles, D., O'Neill, N.T., Tsay, S.C., Ji, Q., Al Mandoos, A., Ramzan Khan, M., Reid, E.A., Schafer, J.S., Sorokine, M., Newcomb, W., Slutsker, I., 2008. Spatial and temporal variability of column-integrated aerosol optical properties in the Southern Arabian Gulf and United Arab Emirates in summer. J. Geophys. Res. 113, D01204. doi:10.1029/2007JD008944.

El-Metwally, M., Alfaro, S.C., Abdel Wahab, M., Chatenet, B., 2008. Aerosol characteristics over urban Cairo: seasonal variations as retrieved from Sun photometer measurements. J. Geophys. Res. 113, D14219. doi:10.1029/2008JD009834.

Engelstaedter, S., Tegen, I., Washington, R., 2006. North African dust emissions and transport. Earth-Sci. Rev. 79 (1,2), 73–100.

Fairlie, T.D., Jacob, D.J., Park, R.J., 2007. The impact of transpacific transport of mineral dust in the United States. Atmos. Environ. 7, 1251–1266.

Feng, Q., Yang, P., Kattawar, G.W., Hsu, C.N., Tsay, S.C., Laszlo, I., 2009. Effects of particle nonsphericity and radiation polarization on retrieving dust properties from MODIS observations. J. Aerosol Sci. 40, 776–789.

Finlayson-Pitts, B.J., Pitts, J.N., 2000. Chemistry of the Upper and Lower Atmosphere: Theory, Experiments and Applications. Academic Press, New York.

Fluckiger, D.U., Lin, H.-B., Marlow, W.H., 1985. Composition measurement of aerosols of submicrometer particles by phase fluctuation absorption spectroscopy. Appl. Opt. 24, 1668–1681.

Fukagawa, S., Kuze, H., Lagrosas, N., Takeuchi, N., 2005. High efficiency aerosol scatterometer that uses an integrating sphere for the calibration of multiwavelength LIDAR data. Appl. Opt. 44, 3520–3526.

Gasteiger, J., Wiegner, M., Toledano, C., Koepke1, P., 2009. Effects of complex shapes on radiative properties of mineral dust aerosol: Implications on sun photometry. European Aerosol Conference 2009, Karlsruhe, Abstract T047A03.

Gayet, J.F., Crepel, O., Fournol, J.F., Oshchepkov, S., 1997. A new airborne polar nephelometer for the measurements of optical and microphysical cloud properties. Part I. Theoretical design. Ann. Geophys. 15, 451–459.

Gogoi, A., Borthakur, L.J., Choudhury, A., Stanciu, G.A., Ahmed, G.A., 2009. Detector array incorporated optical scattering instrument for nephelometric measurements on small particles. Meas. Sci. Technol. 20, 095901. doi:10.1088/0957-0233/20/9/095901.

Goudie, A.S., Middleton, N.J., 2001. Saharan dust storms: nature and consequences. Earth-Sci. Rev. 56 (1–4), 179–204.

Haywood, J., Francis, P., Osborne, S., Glew, M., Loeb, N., Highwood, E., Tanre, D., Myhre, G., Formenti, P., Hirst, E., 2003. Radiative properties and direct radiative effect of Saharan dust measured by the C-130 aircraft during SHADE: 1. Solar spectrum. J. Geophys. Res. 108 (D18), 8577. doi:10.1029/2002JD002687.

Heintzenberg, J., Wiedensohler, T.M., Tuch, T.M., Covert, D.S., Sheridan, P.S., Ogren, J.A., Gras, J., Nessler, R., Kleefeld, C., Kalivitis, N., Aaltonen, V., Wilhem, R.T., Havlicek, M., 2006. Intercomparisons and aerosol calibrations of 12 commercial integrating nephelometers of three manufacturers. J. Atmos. Ocean. Technol. 23, 902–914.

Hinds, W.H., 1999. Aerosol Technology: Properties, Behavior and Measurements of Airborne Particles, second ed. John Wiley & Sons, New York.

Hu, R.M., Sokhi, R.S., 2009. Light scattering and absorption properties of dust particles retrieved from satellite measurements. J. Quant. Spectrosc. Rad. Trans. 110, 1698–1705.

Huebert, B.J., Bates, T., Russell, P.B., Shi, G., Kim, Y.J., Kawamura, K., Carmichael, G., Nakajima, T., 2003. An overview of ACE-Asia: strategies for quantifying the relationships between Asian aerosols and their climatic impacts. J. Geophys. Res. 108 (23), D8633. doi:10.1029/2003JD003550.

Hwang, H., Ro, C.-U., 2005. Single-particle characterization of four aerosol samples collected in ChunCheon, Korea, during Asian dust storm events in 2002. J. Geophys. Res. 110, D23201. doi:10.1029/2005JD006050.

Hwang, H., Ro, C., 2006. Direct observation of nitrate and sulfate formations from mineral dust and seas-salts using low-Z particle electron probe X-ray microanalysis. Atmos. Environ 40, 3869–3880.

Immler, F., Engelbart, D., Schrems, O., 2005. Fluorescence from atmospheric aerosol detected by a lidar indicates biogenic particles in the lowermost stratosphere. Atmos. Chem. Phys. 5, 345–355.

Jaffe, D.A., Anderson, T., Covert, D., Kotchenruther, R., Trost, B., Danielson, J., Simpson, W., Bernstein, T., Karlsdottir, S., Blake, D., Harris, J., Carmichel, G., Itsushi, U., 1999. Transport of Asian air pollution to North America. Geophys. Res. Lett. 26, 711–714. doi:10.1029/1999GL900100.

Jaffe, D.A., McKendry, I., Anderson, T., Price, H., 2003a. Six new episodes of trans-Pacific transport of air pollutants. Atmos. Environ. 37, 391–404. doi:10.1016/S1352-2310(02)00862-2.

Jaffe, D.A., Snow, J., Cooper, O., 2003b. The 2001 Asian dust events: transport and impact on surface aerosol concentrations in the US. Eos Trans. AGU 84 (46), 501–516. doi:10.1029/2003EO460001.

Jickells, T.D., An, Z.S., Andersen, K.K., Baker, A.R., Bergametti, G., Brooks, N., Cao, J.J., Boyd, P.W., Duce, R.A., Hunter, K.A., Kawahata, H., Kubilay, N., LaRoche, J., Liss, P.S., Mahowald, N., Prospero, J.M., Ridgwell, A.J., Tegen, L., Torres, R., 2005. Global iron connections between desert dust, ocean biogeochemistry, and climate. Science 308, 67–71.

Jin, J., 2002. The Finite Element Method in Electromagnetics. Wiley, New York.

Kandler, K., Benker, N., Bundke, U., Cuevas, E., Ebert, M., Knippertz, P., Rodriguez, S., Schutz, L., Weinbruch, S., 2007. Chemical composition and complex refractive index of Saharan Mineral Dust at Izana, Tenerife (Spain) derived by electron microscopy. Atmos. Environ. 41, 8058–8074.

Kaufman, Y.J., Tanré, D., Dubovik, O., Karnieli, A., Remer, L.A., 2001. Absorption of sunlight by dust as inferred from satellite and ground-based remote sensing. Geophys. Res. Lett. 28 (8), 1479–1482.

Kerker, M., 1969. The Scattering of Light and Other Electromagnetic Radiation. Academic Press, New York.

Kim, S.W., Yoon, S.-C., Dutton, E.G., Kim, J., Wehrli, C., Holben, B.N., 2008. Global surface-based sun photometer network for long-term observations of column aerosol optical properties: intercomparison of aerosol optical depth. Aerosol Sci. Technol. 42 (1), 1–9.

Lack, D.A., Lovejoy, E.R., Baynard, T., Pettersson, A., Ravishankara, A.R., 2006. Aerosol absorption measurement using photoacoustic spectroscopy: sensitivity, calibration, and uncertainty developments. Aerosol Sci. Technol. 40 (9), 697–708.

Lafon, S., Sokolik, I.N., Rajot, J.L., Caquineau, S., Gaudichet, A., 2006. Characterization of iron oxides in mineral dust aerosols: implications for light absorption. J. Geophys. Res.-Atmos. 111. doi:10.1029/2005JD007016.

Lang-Yona, N., Rudich, Y., Segre, E., Dinar, E., Abo-Riziq, A., 2009. Complex refractive indices of aerosols retrieved by continuous wave-cavity ring down aerosol spectrometer. Anal. Chem. 81 (5), 1762–1769.

Laurent, B., Marticorena, B., Bergametti, G., Léon, J.F., Mahowald, N.M., 2008. Modeling mineral dust emissions from the Sahara desert using new surface properties and soil database. J. Geophys. Res. 113, D14218. doi:10.1029/2007JD009484.

Lee, J.A., Gill, T.E., Mulligan, K.R., Dominguez Acosta, M., Perez, A.E., 2009. Land use/land cover and point sources of the 15 December 2003 dust storm in southwestern North America. Geomorphology 105, 18–27.

Lewis, E.R., Schwartz, S.E. 2004. Sea Salt Aerosol Production: Mechanisms, Methods, Measurements, and Models: A Critical Review. Geophysical Monograph, vol. 152, American Geophysical Union, Washington DC, 413p, ISBN: 0-87590-417-3.

Lewis, K., Arnott, W.P., Moosmuller, H., Wold, C.E., 2008. Strong spectral variation of biomass smoke light absorption and single scattering albedo observed with a novel dual-wavelength photoacoustic instrument. J. Geophys. Res. Atmos. 113 (D16), D16203.

Li, L.W., Kang, X.K., Leong, M.S., 2002. Spheroidal Wave Functions in Electromagnetic Theory. Wiley, New York.

Lienert, B.R., Porter, J.N., Sharma, S.K., 2003. Aerosol size distributions from genetic inversion of polar nephelometer data. J. Atmos. Oceanic Technol. 20 (10), 1403–1410.

Linke, C., Mohler, O., Veres, A., Mohacsi, A., Bozoki, Z., Szabo, G., Schnaiter, M., 2006. Optical properties and mineralogical composition of different Saharan mineral dust samples: a laboratory study. Atmos. Chem. Phys. 6, 3315–3323.

Liou, K.N., 2002. An Introduction to Atmospheric Radiation. Elsevier, New York. 583p., ISBN: 978-0-12-451451-5..

Liu, D., Wang, Z., Liu, Z., Winker, D., Trepte, C., 2008. A height resolved global view of dust aerosols from the first year CALIPSO lidar measurements. J. Geophys. Res. 113, D16214. doi:10.1029/2007JD009776.

Lowenthal, D.H., Watson, J.G., Saxena, P., 2000. Contributions to light extinction during project MOHAVE. Atmos. Environ. 34, 2351–2359.

Mackowski, D.W., 2002. Discrete dipole moment method for calculation of the T matrix for nonspherical particles. J. Opt. Soc. Am. A 19, 881–893.

Mahowald, N.M., Baker, A.R., Bergametti, G., Brooks, N., Duce, R.A., Jickells, T.D., Kubilay, N., Prospero, J.M., Tegen, I., 2005. Atmospheric global dust cycle and iron inputs to the ocean. Global Biogeochem. Cycles 19, GB4025. doi:10.1029/2004GB002402.

Malm, W.C., Persha, G., 1991. Considerations in the accuracy of a long-path transmissometer. Aerosol Sci. Technol. 14 (4), 459–471.

Malm, W.C., Kreidenweis, S.M., 1997. The effects of models of aerosol hygroscopicity on the apportionment of extinction. Atmos. Environ. 31, 1965–1976.

Malm, W.C., Day, D.E., Kreidenweis, S.M. 1997. Comparison of measured and reconstructed scattering during an intensive field study at Great Smoky Mountains National Park, paper #97-WA70.02, presented at the Air and Waste Management 90th Annual Meeting, Pittsburgh, PA.

Martin, R.V., 2008. Satellite remote sensing of surface air quality. Atmos. Environ. 42, 7823–7843.

McConnell, C.L., Highwood, E.J., Coe, H., Formenti, P., Anderson, B., Osborne, S., Nava, S., Desboeufs, K., Chen, G., Harrison, M.A., 2008. Seasonal variations of the physical and optical characteristics of Saharan dust: results from the dust outflow and deposition to the ocean (DODO) experiment. J. Geophys. Res. 113, D14S05. doi:10.1029/2007JD009606.

Menon, S., Hansen, J., Nazarenko, L., Luo, Y., 2002. Climate effects of black carbon aerosols in China and India. Science 297 (5590), 2250–2253.

Miller, J.L., Orr-Ewing, A.J., 2007. CRDS measurements of single aerosol particle extinction. Part 2. Extinction of light by an aerosol particle in an optical cavity excited by a cw laser. J. Chem. Phys. 126, 174303.

Miller, T.M., Grassian, V.H., 1998. Heterogeneous chemistry of NO_2 on mineral oxide particles: spectroscopic evidence for oxide-coordinated and water solvated surface nitrate. Geophys. Res. Lett. 25, 3835–3838.

Mikami, M., Shi, G.Y., Uno, I., Yabuki, S., Iwasaka, Y., Yaui, M., Aoki, T., Tanaka, T.Y., Kurosaki, Y., Masuda, K., Uchiyama, A., Matsuki, A., Sakai, T., Takemi, T., Nakawo, M., Seino, N., Ishizuka, M., Satake, S., Fujita, K., Hara, Y., Kai, K., Kanayama, S., Hayashi, M., Du, M., Kanai, Y., Yamada, Y., Zhang, X.Y., Shen, Z., Zhou, H., Abe, O., Nagai, T., Tsutsumi, Y., Chiba, M., Suzuki, J., 2006. Aeolian dust experiment on climate impact: an overview of Japan–China joint project ADEC global and planet. Change 52, 142–172.

Mishchenko, M.I., Travis, L.D., Mackowski, D.W., 1996. T-matrix computations of light scattering by nonspherical particles: a review. J. Quant. Spectros. Radiat. Transfer. 55 (5), 535–575.

Mishchenko, M.I., Hovenier, J.W., Travis, L.D. (Eds.), 2000. Light Scattering by Nonspherical Particles: Theory, Measurements, and Applications. Academic Press, San Diego.

Mishchenko, M.I., Travis, L.D., Lacis, A.A., 2002. Scattering, Absorption, and Emission of Light by Small Particles. Cambridge University Press, Cambridge, UK.

Mishchenko, M.I., Videen, G., Babenko, V.A., Khlebtsov, N.G., Wriedt, T., 2007. Comprehensive T-matrix reference database: a 2004–2006 update. J. Quant Spectrosc. Radiat. Transfer 106, 304–324.

Mishchenko, M.I., Videen, G., Khlebtsov, N.G., Wriedt, T., Zakharova, N.T., 2008. Comprehensive T-matrix reference database: a 2006–2007 update. J. Quant. Spectrosc. Radiat. Transfer 109, 1447–1460.

Molenar, J.V., Persha, G., Malm, W.C. 1989a. Long path transmissometer for measuring ambient atmospheric extinction. In: Mathai, C.V. (Ed.), Transactions of Visibility and Fine Particles, Air and Waste Management Association, Pittsburgh, PA, pp. 293–304.

Molenar, J.V., Dietrich, D.L., Tree, R.M., Malm, W.C., Persha, G., 1989b. Application of a long range transmissometer to measure ambient atmospheric extinction coefficient in remote pristine environments. In: Mathai, C.V. (Ed.), Transactions of Visibility and Fine Particles, Air and Waste Management Association: Pittsburgh, PA, pp. 305–317.

Moorthy, K.K., Babu, S.S., Satheesh, S.K., Srinivasan, J., Dutt, C.B.S., 2007. Dust absorption over the Great Indian Desert inferred using ground-based and satellite remote sensing. J. Geophys. Res. 112, D09206. doi:10.1029/2006JD007690.

Moosmüller, H., Varma, R., Arnott, W., 2005. Cavity ring-down and cavity-enhanced detection techniques for the measurement of aerosol extinction. Aerosol Sci. Technol. 39 (1), 30–39.

Moosmüller, H., Chakrabarty, R.K., Arnott, W.P., 2009. Aerosol light absorption and its measurement: a review. J. Quant. Spectrosc. Radiat. Transfer 110, 844–878.

Müller, T., Schladitz, A., Massling, A., Kaaden, N., Kandler, K., Wiedensohler, A., 2009a. Spectral absorption coefficients and imaginary parts of refractive indices of Saharan dust during SAMUM-1. Tellus B 61 (1), 79–95.

Müller, T., Petzold, A., Rasp, K., Schladitz, A., Vragel, M., Schnaiter, M. Linke, C. 2009b. Spectral Absorption of Mineral Dust: Results of the Mineral Dust Campaign 2008 at the AIDA facility, Forschungszentrum Karlsruhe. European Aerosol Conference 2009, Karlsruhe, Abstract T052A12.

Muñoz, O., Volten, H., de Haan, J.F., Vassen, W., Hovenier, J.W., 2001. Experimental determination of scattering matrices of randomly oriented fly ash and clay particles at 442 and 633 nm. J. Geophys. Res. 106, 22833–22844.

Nieminen, T.A., Rubinsztein-Dunlop, H., Heckenberg, N.R., 2003. Calculation of the T-matrix: general considerations and application of the point-matching method. J. Quant. Spectrosc. Radiat. Transfer 79–80, 1019–1029.

Nousiainen, T., 2009. Optical modeling of mineral dust particle: a review. J. Quant. Spectros. Radiat. Trans. 110 (14–16), 1261–1279.

Olson, L.W., Boison, K., 2005. Health impact and control of particle matter. In: Nicolopoulou-Stamati, P. et al. (Eds.), Enironmental Health Impacts of Transport and Mobility. Springer, The Netherlands, pp. 115–125.

Optec, Inc., 2005. LPV-3 Technical Manual for Theory of Operation and Operating Procedures. Lowell, MI 49331.

Osborne, S.R., Johnson, B.T., Haywood, J.M., Baran, A.J., Harrison, M.A.J., McConnell, C.L., 2008. Physical and optical properties of mineral dust aerosol during the dust and biomass-burning experiment. J. Geophys. Res. 113, D00C03. doi:10.1029/2007JD009551.

Pan, Y.-L., Pinnick, R.G., Hill, S.C., Rosen, J.M., Chang, R.K., 2007. Single-particle laser-induced-fluorescence spectra of biological and other organic-carbon aerosols in the atmosphere: measurements at New Haven, Connecticut and Las Cruces, New Mexico. J. Geophys. Res. 112, D24S19. doi:10.1029/2007JD008741.

Pandithurai, G., Dipu, S., Dani, K.K., Tiwari, S., Bisht, D.S., Devara, P.C.S., Pinker, R.T., 2008. Aerosol radiative forcing during dust events over New Delhi, India. J. Geophys. Res. 113, D13209. doi:10.1029/2008JD009804.

Penttila, A., Zubko, E., Lumme, K., Muinonen, K., Yurkin, M.A., Draine, B.T., Rahola, J., Hoekstra, A.G., Shkuratov, Y., 2007. Comparison between discrete dipole implementations and exact techniques. J. Quant. Spectrosc. Radiat. Transfer 106, 417–436.

Petzold, A., Rasp, K., Weinzierl, B., Esselborn, M., Hamburger, T., Dornbrack, A., Kandler, K., Schutz, L., Knippertz, P., Fiebig, M., Virkkula, A., 2009. Saharan dust absorption and refractive index from aircraft-based observations during SAMUM 2006. Tellus B 61 (1), 118–130.

Petzold, A., Schonlinner, M., 2004. Multi-angle absorption photometry – a new method for the measurement of aerosol light absorption and atmospheric black carbon. J. Aerosol Sci. 35 (4), 421–441.

Purcell, M., Pennypacker, C.R., 1973. Scattering and absorption of light by nonspherical dielectric grains. Astrophys. J. 186, 705–714.

Qin, Y., Mitchell, R.M., 2009. Characterisation of episodic aerosol types over the Australian continent. Atmos. Chem. Phys. 9, 1943–1956.

Reid, J.S., Hobbs, P.V., Liousse, C., Vanderlei Martins, J., Weiss, R.E., Eck, T.F., 1998. Comparisons of techniques for measuring shortwave absorption and black carbon content of aerosols from biomass burning in Brazil. J. Geophys. Res. 103, 32031–32040.

Salam, A., Lohmann, U., Crenna, B., Lesins, G., Klages, P., Rogers, D., Irani, R., MacGillivray, A., Coffin, M., 2006. Ice nucleation studies of mineral dust particles with a new continuous flow diffusion chamber. Aerosol Sci. Technol. 40, 134–143.

Sarnat, J.A., Loutrakis, P., Suh, H., 2000. Assessing the relationship between personal particulate and gaseous exposures of senior citizens living in Baltimore, MD. J. Air Waste Manage. Assoc. 50, 1184–1198.

Schladitz, A., Muller, N., Kaaden, N., Massling, A., Kandler, K., Ebert, M., Weinbruch, S., Deutscher, C., Wiedensohler, A., 2009. In situ measurements of optical properties at Tinfou (Morocco) during the Saharan Mineral Dust Experiment SAMUM 2006. Tellus B 61 (1), 64–78.

Schmid, B., Matzler, C., 1997. Retrieval of optical depth and particle size distribution of tropospheric and stratospheric aerosols by means of Sun photometry. IEEE Trans. Geosci. Rem. Sens. 35 (1), 172–182.

Schmid, O., Artaxo, P., Arnott, W.P., Chand, D., Gatti, L.V., Frank, G.P., Hoffer, A., Schnaiter, M., Andreae, M.O., 2006. Spectral light absorption by ambient aerosols influenced by biomass burning in the Amazon Basin I: comparison and field calibration of absorption measurement techniques. Atmos. Chem. Phys. 6, 3443–3462.

Sedlacek, A.J., 2006. Real-time detection of ambient aerosols using photothermal interferometry: folded Jamin interferometer. Rev. Sci. Instrum. 77, 064903.

Sedlacek, A.J., Lee, J., 2007. Photothermal interferometric aerosol absorption spectrometry. Aerosol Sci. Technol. 41 (12), 1089–1101.

Sheridan, P.J., Arnott, W.P., Ogren, J.A., Andrews, E., Atkinson, D.B., Covert, D.S., Moosmuller, H., Petzold, A., Schmid, B., Strawa, A.W., Varma, R., Virkkula, A., 2005. The reno aerosol optics study: an evaluation of aerosol absorption measurement methods. Aerosol Sci. Technol. 39, 1–16.

Shi, G., Wang, H., Wang, B., Li, W., Gong, S., Zhao, T., Aoki, T., 2005. Sensitivity experiments on the effects of optical properties of dust aerosols on their radiative forcing under clear sky condition. J Meteorol. Soc. Jpn 83A, 333–346.

Singh, S., Nath, S., Kohli, R., Singh, R., 2005. Aerosols over Delhi during pre-monsoon months: characteristics and effects on surface radiation forcing. Geophys. Res. Lett. 32, L13808. doi:10.1029/2005GL023062.

Singh, R.P., Dey, S., Tripathi, S.N., Tare, V., Holben, B., 2004. Variability of aerosol parameters over Kanpur, Northern India. J. Geophys. Res. 109, D23206. doi:10.1029/2004JD004966.

Sloane, C.S., 1983. Optical properties of aerosols-comparison of measurements with model calculations. Atmos. Environ. 17, 409–416.

Sloane, C.S., 1984. Optical properties of aerosols of mixed composition. Atmos. Environ. 18, 871–878.

Sloane, C.S., Wolff, G.T., 1985. Change in aerosol optical properties with change in chemical composition. Atmos. Environ. 19, 669–680.

Smith, J.D., Atkinson, D.B., 2001. A portable pulsed cavity ring-down transmissometer for measurement of the optical extinction of the atmospheric aerosol. Analyst 126, 1216.

Sokolik, I.N., Golitsyn, G., 1993. Investigation of optical and radiative properties of atmospheric dust aerosols. Atmos. Environ. 37, 2509–2517.

Sokolik, I.N., Toon, O.B., 1999. Incorporation of mineralogical composition into models of the radiative properties of mineral aerosol from UV to IR wavelengths. J. Geophys. Res. 104 (D8), 9423–9444.

Strawa, A.W., Castaneda, R., Owano, T., Baer, D.S., Paldus, B.A., 2003. The measurement of aerosol optical properties using continuous wave cavity ring-down techniques. J. Atmos. Ocean. Technol. 20, 454–465.

Sullivan, R.C., Guazzotti, S.A., Sodeman, D.A., Prather, K.A., 2007. Direct observations of the atmospheric processing of Asian mineral dust. Atmos. Chem. Phys. 7, 1213–1236.

Taflove, A., Hagness, S.C., (2000). Computational electrodynamics: the finite-difference time-domain method. Artech House, Boston.

Tanré, D., Haywood, J., Pelon, J., Le'on, J.F., Chatenet, B., Formenti, P., Francis, P., Goloub, P., Highwood, E.J., Myhre, G., 2003. Measurement and modeling of the Saharan dust radiative impact: overview of the Saharan Dust Experiment (SHADE). J. Geophys. Res. 108 (D18), 8574. doi:10.1029/2002JD003273.

Textor, C., Schulz, M., Guibert, S., Kinne, S., Balkanski, Y., Bauer, S., Berntsen, T., Berglen, T., Boucher, O., Chin, M., Dentener, F., Diehl, T., Easter, R., Feichter, H., Fillmore, D., Ghan, S., Ginoux, P., Gong, S., Grini, A., Hendricks, J., Horowitz, L., Huang, P., Isaksen, L., Iversen, T., Kloster, S., Koch, D., Kirkevag, A., Kristjansson, J.E., Krol, M., Lauer, A., Lamarque, J.F., Liu, X., Montanaro, V., Myhre, G., Penner, P., Pitari, G., Reddy, S., Seland, Ø., Stier, P., Takemura, T., Tie, X., 2006. Analysis and quantification of the diversities of aerosol life cycles within AeroCom. Atmos. Chem. Phys. 6, 1777–1813.

Thompson, J.E., Smith, B.W., Winefordner, J., 2002. Monitoring atmospheric particulate matter through cavity ring-down spectroscopy. Anal. Chem. 74, 1962–1967.

Thompson, J.E., Nasajpour, H., Smith, B.W., Winefordner, J., 2003. Atmospheric aerosol measurement by cavity ringdown turbidimetry. Aerosol Sci. Technol. 37, 221–230.

Thompson, J.E., Barta, N., Policarpio, D., DuVall, R., 2008. A fixed frequency aerosol albedometer. Opt. Express 16, 2191–2205.

Todd, M.C., Washington, R., Vanderlei Martins, J., Dubovik, O., Lizcano, L., M'Bainayel, S., Engelstaedter, S., 2007. Mineral dust emission from the Bodélé Depression, Northern Chad, during BoDEx 2005. J. Geophys. Res. 112, D06207. doi:10.1029/2006JD007170.

Toon, O.B., 2003. African dust in Florida clouds. Nature 424, 623–624.

Uchiyama, A., Yamazaki, A., Togawa, H., Asano, J., 2005a. Characteristics of aeolian dust observed by sky-radiometer in the intensive observation Period 1 (IOP1). J. Meteorol. Soc. Jpn 83A, 291–305.

Uchiyama, A., Yamazaki, A., Togawa, H., Asano, J., Shi, G., 2005b. Single scattering albedo of aeolian dust as inferred from sky-radiometer and in situ ground-based measurement. SOLA 1, 209–219. doi:10.2151/sola.2005-054.

Usher, C.R., Michel, A.E., Grassian, V.H., 2003. Reactions on mineral dust. Chem. Rev. 103, 4883–4940.

Varma, R., Moosmuller, H., Arnott, W.P., 2003. Toward an ideal integrating nephelometer. Opt. Lett. 28 (12), 1007–1009.

Virkkula, A., Ahlquist, N.C., Covert, D.S., Sheridan, P.J., Arnott, W.P., Ogren, J.A., 2005. A three-wavelength optical extinction cell for measuring aerosol light extinction and its application to determining light absorption coefficient. Aerosol Sci. Technol. 39, 52–67.

Volten, H., Muñoz, O., de Haan, J.F., Vassen, W., Hovenier, J.W., Muinonen, K., 2001. Scattering matrices of mineral aerosol particles at 441.6 nm and 632.8 nm. J. Geophys. Res. 106, 17375–17401.

Waterman, P.C., 1965. Matrix formulation of electromagnetic ccattering. In: Proc. IEEE 53, pp. 805–812.

Waterman, P.C., 1971. Symmetry, unitarity, and geometry in electromagnetic scattering. Phys. Rev. D 3, 825–839.

Weingartner, E., Saathoff, H., Schnaiter, M., Streit, N., Bitnar, B., Baltensperger, U., 2003. Absorption of light by soot particles: determination of the absorption coefficient by means of aethalometers. J. Aerosol Sci. 34 (10), 1445–1463.

Weiss, R.E., Hobbs, P.V., 1992. Optical extinction properties of smoke from the Kuwait oil fires. J. Geophys. Res. 97 (D13), 14537–14540.

Wilson, W.E., Reist, P.C., 1994. A PC-based Mie scattering program for theoretical investigations of the optical properties of atmospheric aerosols as a function of composition and relative humidity. Atmos. Env. 28, 803–809.

WMO, 1983: Radiation Commission of IAMAP Meeting of Experts on Aerosol and Their Climatic Effects, WCP55, Williamsburg VA, pp. 28–30.

Wriedt, T. (Ed.), 1999. Generalized Multipole Techniques for Electromagnetic and Light Scattering. Elsevier, Amsterdam.

Yee, S.K., 1966. Numerical solution of initial boundary value problems involving Maxwell's equations in isotropic media. IEEE Trans. Antennas Propag. 14, 302–307.

Yurkin, M.A., Hoekstra, A.G., 2007a. The discrete dipole approximation: an overview and recent developments. J. Quant. Spectros. Radiat. Trans. 106 (1-3), 558–589.

Yurkin, M.A., Maltsev, V.P., Hoekstra, A.G., 2007b. The discrete dipole approximation for simulation of light scattering by particles much larger than the wavelength. J. Quant. Spectros. Radiat. Transfer 106 (1–3), 546–557.

Zhang, X.Y., Gong, S.L., Zhao, T.L., Arimoto, R., Wang, Y.Q., Zhou, Z.J., 2003. Sources of Asian dust and role of climate change versus desertification in Asian dust emission. Geophys. Res. Lett. 30 (24), 2272. doi:10.1029/2003GL018206.

Zuberi, B., Bertram, A.K., Cassa, C.A., Molina, L.T., Molina, M.J., 2002. Heterogeneous nucleation of ice in $(NH_4)_2SO_4$–H_2O particles with mineral dust immersions. Geophys. Res. Lett. 29 (10), 1504. doi:10.1029/2001GL014289.